Orographic Land–Atmosphere Interactions and the Diurnal Cycle of Low-Level Clouds and Fog

ANNA M. WILSON[a] AND ANA P. BARROS

Civil and Environmental Engineering Department, Pratt School of Engineering, Duke University, Durham, North Carolina

ABSTRACT

Previous work illuminated landform controls on moisture convergence in the southern Appalachian Mountains (SAM) promoting heterogeneity in the vertical structure of low-level clouds (LLC) and seeder–feeder interactions (SFI) that significantly impact warm season precipitation. Here, the focus is on elucidating orographic land–atmosphere interactions associated with the observed diurnal cycle of LLC and fog in the region. Three distinct hydrometeorological regimes during the Integrated Precipitation and Hydrology Experiment (IPHEx) are examined using the Weather Research and Forecasting Model. Sensitivity to the choice of planetary boundary layer parameterization was investigated in the light of IPHEx observations. Simulations using the Mellor–Yamada–Nakanishi–Niino scheme exhibit LLC and fog patterns most consistent with observations, albeit without capturing SFI. Independently of synoptic regime, the simulations reveal two distinct modes of orographic controls on atmospheric moisture convergence patterns that explain the diurnal cycle of LLC and fog. First, a stationary nocturnal mode at the meso-α scale associated with an extended flow separation zone supports low-level pooling and trapping of cold, moist, stable air in the inner mountain on the lee side of the western topographic divide. Second, a dynamic daytime mode that results from the coorganization of ridge–valley circulations at the meso-γ scale and Rayleigh–Bénard convection at the meso-β scale is associated with widespread low-level instability below the envelope orography. Orographic decoupling results in the formation of a shallow stagnation zone between the western and eastern topographic divides at night that contracts westward during daytime. Predominantly easterly and southeasterly low-level moisture convergence patterns support early afternoon LLC formation in the inner SAM.

1. Introduction

Prat and Barros (2010), Wilson and Barros (2014, hereafter WB14), Angulo-Martínez and Barros (2015), and Duan et al. (2015) documented evidence of diurnal cycles of precipitation in the southern Appalachian Mountains (SAM; Figs. 1a,b) with strong seasonality and mountain–valley gradients related to the spatiotemporal variability of precipitation microphysics. WB14 reported a robust warm season diurnal cycle of light rainfall associated with low-level cloud and fog (LLCF) immersion in the absence of synoptic-scale forcing. They also elucidated the role of seeder–feeder interactions in enhancing coalescence processes at low

elevations and the intensification of valley rainfall up to one order of magnitude, the reverse orographic effect, in the inner SAM (Wilson and Barros 2015, hereafter WB15). Observations of lateral precipitation presented by WB15 also suggest a strong diurnal cycle of LLCF immersion on the western ridges peaking in the early morning independently of storm activity, and out of phase with the inner-region valleys where it peaks in the early afternoon (Fig. 3b in WB15). For the relatively dry season of 2014, during the Integrated Precipitation and Hydrology Experiment (IPHEx), immersion rainfall at station location P4 (Fig. 1b) exceeded 60% of the total monthly rainfall accumulation, which highlights its importance in the regional water cycle and the sustainability of forest ecosystems, especially in drought conditions.

The SAM region is a perhumid temperate rain forest (Shanks 1954) with areas of temperate mountain cloud forest (Reinhardt and Smith 2008). Perhumid is the wettest climate category according to Thornthwaite (1948). There is some controversy over this classification

[a] Current affiliation: Center for Western Weather and Water Extremes, Scripps Institution of Oceanography, University of California, San Diego, La Jolla, California.

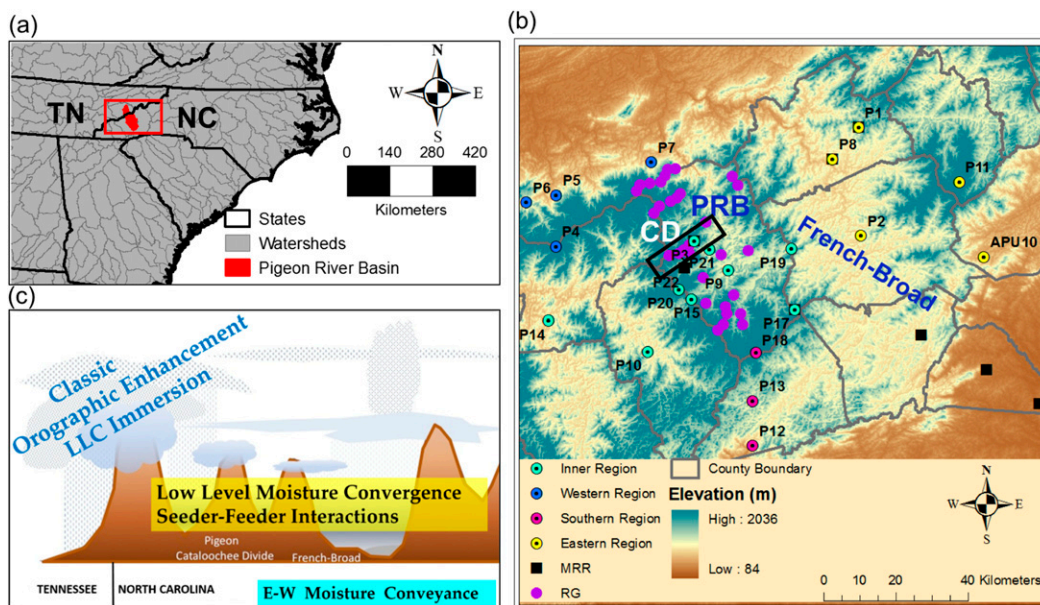*Corresponding author*: Ana P. Barros, barros@duke.edu

FIG. 1. (a) Map of the area of study shown in context of the southeastern United States. The PRB is delineated in red. The red square delimits the region covered in (b). (b) Topography of the study region with instrument locations during IPHEx [rain gauges (RG) are shown by purple circles; PARSIVEL disdrometers are shown by yellow, cyan, blue, and red circles with black dot at the center; micro rain radars (MRRs) are shown by black squares; and Cataloochee Divide (CD) is indicated in white]. (c) Synthesis of key precipitation processes across the SAM after WB14 and WB15. Multilayer clouds are represented by various shades of blue and gray. Darker shades are indicative of higher hydrometeor concentrations.

of the SAM forests, since the region is warmer than temperate rain forests generally, and considerably drier during the summer. Nevertheless, significant precipitation (up to 25% of annual) falls during the driest quarter (WB14), and persistent rain forest–like characteristics in the SAM appear in island-like cove forests throughout the mountains (DellaSala et al. 2011). Albeit at lower elevations, these areas exhibit similarities to tropical cloud forests.

Atmospheric moisture convergence and classical orographic modulation of the lifting condensation level (LCL) are essential processes governing the diurnal cycle of cloud formation in high-elevation cloud forests. In the tropical Andes, evapotranspiration amounts to a small fraction of wet season precipitation, but plays a critical role in low-level entropy gradients, which control convective instability and upslope moisture convergence at regional scale (Sun and Barros 2015b). Elsewhere, evapotranspiration can be an important highly localized moisture source in mountain regions, with patterns modulated by the joint distribution of topography and vegetation (e.g., Dyer 2009; Bhushan and Barros 2007). Mountain circulations also drive variations in the diurnal cycle of aerosol, with consequences on moist processes (Shrestha et al. 2010). Activated CCN and moisture availability are two requisites to maintain the levels of

cloudiness and precipitation observed in the SAM. The focus here is on moisture availability.

The role of high topography and elevated plateaus as heat sources on the one hand and obstacles to airflow on the other, including blocking at multiple spatial scales conditional on environmental stability, has long been studied in the case of massive mountain ranges, such as the Himalayas, the Andes, and the Rockies (e.g., Smith 1979; Wallace 1983). Remote and regional moisture transport modes determine the spatial patterns of evapotranspiration and rainfall in mountainous regions at mountain scale (e.g., Sun and Barros 2015a,b), whereas topography modulates the spatial and temporal organization of cloudiness and precipitation at the ridge–valley scale (Barros et al. 2004; Giovannettone and Barros 2008, 2009). Moisture convergence, cloudiness, and precipitation patterns are tied in fundamental ways to terrain effects on low-level flow and near-surface processes throughout all seasons, but the specific ties can vary significantly depending upon geography and prevailing synoptic-scale patterns, among other effects. That is, the fundamental processes driving precipitation patterns are the same, but their relative roles and interactions change depending upon highly localized landform characteristics. For instance, Wagner et al. (2015) found that mass transport can be up to four times

more efficient across valleys than over flat terrain and is strongest for deep and narrow valleys.

The SAM are midmountains (Clark 2009) characterized by rugged topography with moderate elevations and complex horizontal topology with extensive longitudinal ridges along the southwest–northeast direction, crossed by lower-elevation southeast–northwest ridges, forming wide gaps such as the French Broad valley and enclosed basins such as the Pigeon River basin (PRB; Fig. 1b). The detection and attribution of specific modes of variability to terrain forcing is therefore challenging because of multiple interacting flow features in the lower troposphere. Furthermore, terrain elevations (below 750 hPa) are not high enough to establish significant heating anomalies and, particularly in the warm season, large-scale circulations and regional environmental conditions are not favorable to blocking. The fluid mechanics' analog of large-scale circulation past midmountains is that of flow past an immersed object, which results in flow separation, or mechanical decoupling of the boundary layer from free atmosphere flows due to the establishment of an adverse pressure gradient near the ground (Oke 1978). Local boundary layer development depends on the topography as well as the immersion flow characteristics. Near the land–atmosphere interface, mechanical decoupling is modulated by the diurnal cycle of radiative forcing as well as thermodynamics. Climatological evidence of the orographic decoupling effect (Whiteman 2000) and its signature on point observations of air temperature at the ridge–valley scale (e.g., Daly et al. 2010) is amply documented in the literature.

This work investigates the mechanisms of orographic land–atmosphere interactions associated with the observed diurnal cycle of warm rainfall in the SAM, including reverse orographic enhancement and cloud immersion. WB15 showed that patterns of moisture convergence in weak and strong synoptic forcing conditions modified by the terrain result in "hot spots" consistent with LLCF formation patterns that support seeder–feeder interactions with propagating precipitation systems as proposed by WB14. From observations (WB14; WB15), a synthesis of characteristic regional processes was developed across the SAM (Fig. 1c). The specific objectives of the present work are as follows: 1) to elucidate the diurnal cycle of LLCF including vertical and horizontal structure (ridge–valley contrasts) independently of synoptic forcing conditions; 2) to characterize the relative contributions of remote (moisture advection) and local (evapotranspiration) sources of moisture to LLCF; and 3) to investigate pathways of orographic land–atmosphere interactions that explain the observed resilience of LLCF immersion on diurnal time scales in the absence of large-scale moisture transport (i.e., drought conditions; WB14;

WB15). High-resolution simulations of IPHEx hydrometeorological regimes using the Advanced Research version of the Weather Research and Forecasting Model (ARW; Skamarock et al. 2008) enable assessing moist processes and orographic decoupling impacts on the diurnal cycle of moisture availability in the lower troposphere. Ultimately, the goal is to explain the space–time variability of LLCF and precipitation microphysics in relation to landform and land surface heterogeneity that affects boundary layer processes within the SAM.

2. WRF simulations: Methodology

The WRF simulations were conducted on the National Center for Atmospheric Research's Yellowstone system (NCAR 2012). For consistency with WB15, the WRF version used was 3.5.1. The model was implemented using three one-way nested domains, at 9-, 3-, and 1-km resolution (Fig. 2a). The terrain representation was modified from the standard WRF 1-km terrain, where smoothing can affect ridge–valley circulations and transport (Barros et al. 2004; Wagner et al. 2015). Specifically, the 1-km WRF topography used in these simulations was obtained from the 30-m terrain available from the USGS digital elevation model (Dollison 2010) using the fractal upscaling method described in Bindlish and Barros (1996). The new topography along cross section $D–D'$ marked in Fig. 2b, a subset of domain 3 centered in the PRB, is shown in Fig. 2c for comparison against the WRF standard terrain from WB15 (old). The model grid has 60 vertical levels, with 14 levels in the lowest kilometer, following Sun and Barros (2015a).

The WRF configuration in the simulations includes Milbrandt microphysics (Milbrandt and Yau 2005a,b), Noah land surface (Ek et al. 2003), Kain–Fritsch cumulus parameterization in the first domain only (Kain 2004), RRTM longwave radiation (Mlawer et al. 1997), and the Dudhia shortwave scheme (Dudhia 1989). The selection of Milbrandt microphysics follows sensitivity studies conducted by WB15 with a focus on the model's ability to simulate LLCF in the inner SAM. Milbrandt is a double-moment bulk microphysics parameterization that assumes a gamma drop size distribution (DSD) and predicts the vertical structure of number concentration and mixing ratio for six different hydrometeor types (cloud water, cloud ice, liquid water, snow, graupel, and hail; Milbrandt and Yau 2005a). Thus, it is possible to evaluate simulated low-level microphysics against disdrometer observations of DSDs at the ground surface during IPHEx. Because the representation of atmospheric processes in the lowest 1 km AGL is key to understanding the role of land–atmosphere interactions in the diurnal cycle of
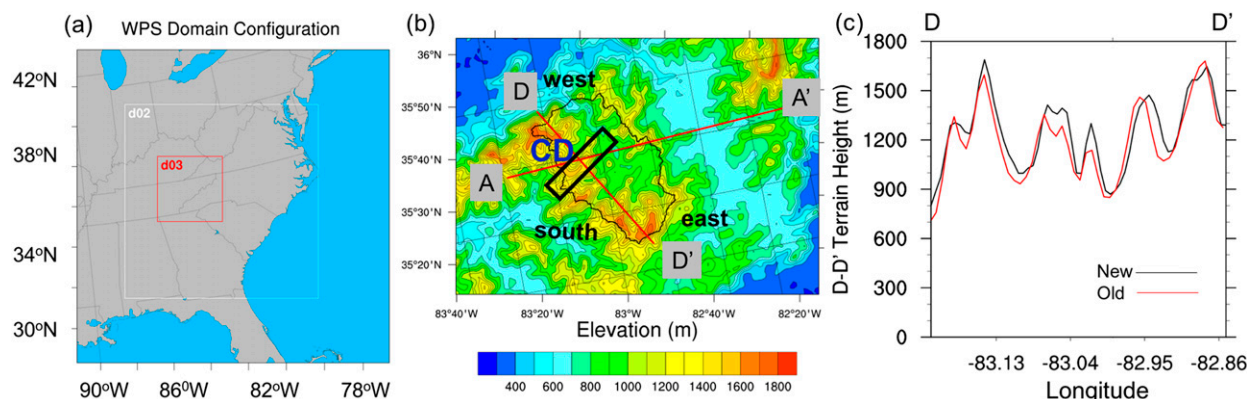
FIG. 2. (a) WRF domains used in the simulations described in this study. (b) Domain 3 terrain upscaled from 3-arc-s resolution using fractal methods after Bindlish and Barros (1996), with the PRB outlined in black and two cross sections A–A′ and D–D′ marked for analysis (the east, west, and south orientations used for discussion of model results are identified for reference). (c) Intercomparison of terrain elevations along D–D′ from domain 3 (new) and the standard WRF terrain (old).

LLCF, a sensitivity analysis of model simulations was conducted using different planetary boundary layer (PBL) parameterizations and their associated surface layer schemes as described in section 3.

Initial and boundary conditions were extracted from the National Centers for Environmental Prediction (NCEP) Final Operational Global Analysis (FNL; Kalnay et al. 1996) as in WB15. These data are available every 6 h on 1° × 1° grids from the Global Data Assimilation System (GDAS) and at 27 levels including the surface in the vertical. This forcing dataset was selected based on Sun and Barros (2012, 2014), where NCEP FNL was reported to capture storm structure and evolution in this region more accurately than North American Regional Reanalysis (NARR), even though NARR is at higher resolution. Simulations were conducted with 6-h spinup in the first domain.

3. Model simulations of hydrometeorological regimes

The three case studies, representative of dominant hydrometeorological regimes during IPHEx, are described in section 3a. Section 3b discusses the sensitivity of the simulated low-level hydrometeorology to the PBL physical parameterizations.

a. Case studies

Three case studies (Table 1) were chosen to represent different warm season interactions between synoptic- and mesoscale circulations during IPHEx (Barros et al. 2014), a ground-validation campaign in support of the Global Precipitation Measurement mission (Hou et al. 2014). An intensive observing period (IOP) was held in the SAM from 1 May to 15 June 2014. The reason behind choosing three events during IPHEx was to leverage quality observations from high-density networks of Particle Size and Velocity (PARSIVEL) disdrometers (Angulo-Martínez and Barros 2015; Tokay et al. 2014, 2013) and tipping-bucket rain gauges (Fig. 1b).

The first case study (case 1, 12–16 May 2014) includes a nighttime frontal passage on 14–15 May as a large-scale synoptic cyclone moved in from the west after a dry period of about one week. Previously, WB15 simulated case 1 and examined moisture convergence patterns. Figures 5 and 7 from WB15 show synoptic weather maps and local observations from this case and are not reproduced here. Rainfall was recorded at all IPHEx stations in the SAM during the frontal passage. During the frontal passage, disdrometer observations at the higher-elevation locations exhibited larger mass-weighted mean diameter D_m values, in particular at the

TABLE 1. Cases.

| Case (2014)	Regional flow	Microphysics	Notes
1: From 12 to 16 May	Westerly	Higher D_m	Light rainfall daily, frontal passage
2: From 17 to 22 May	Southwesterly	Low D_m	Dry weather interrupted by one light rainfall caused by shortwave propagation, inner-region fog observed
3: From 30 May to 6 Jun	Southwesterly/southeasterly	Widespread	Inner-region fog observed, light rainfall events associated with daytime shallow convection
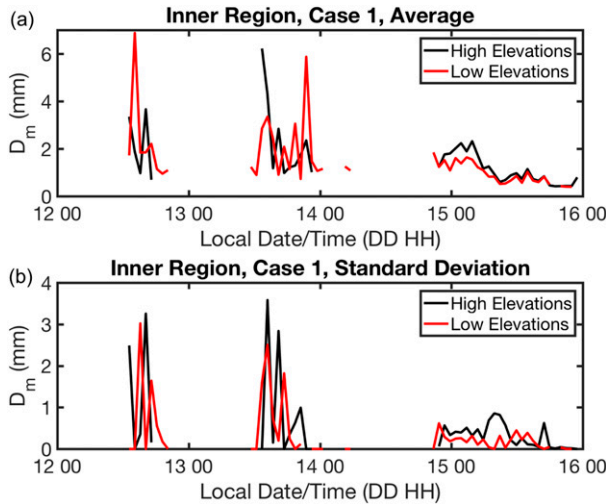
FIG. 3. Time series of D_m statistics derived from observations made by PARSIVEL disdrometers in the inner region (see Fig. 1b, cyan circles with black dot at the center) for case 1 (from 0000 UTC 12 May to 0400 UTC 16 May 2014): (a) average values and (b) std dev. Colors refer to high/low (black/red) elevations.

beginning of the event, in contrast with lighter rainfall events on the previous days (Figs. 3a,b).

The second case (case 2, 17–22 May 2014) begins just one day after the first case. It occurs during a "quiet" period of weak large-scale forcing under northwesterly flow. With mostly dry air entering the region of interest, showers were scattered during this period and based on local forcing, and in the beginning of the period, the presence and propagation of a shortwave from the southwest. After 18 May, high pressure was in place over the region. Photographs of fog conditions and cap clouds at the ground surface in the inner SAM were taken both in the morning and in the evening (e.g., Figs. 4a,b). Observed rainfall totals in the wider IPHEx domain did not exceed 10 mm over the simulated period, and in the inner region (pictured) they did not exceed ~5 mm. In particular, rainfall rates did not exceed 1 mm h^{-1} (Fig. 4c), and a significant difference between high and low elevations was observed at lower rainfall intensities (<0.5 mm h^{-1}) with low-elevation D_m values 30%–50% higher than their high-elevation counterparts (Figs. 4c,d).

The third case occurred from 30 May to 6 June 2014 (case 3). Upper-level flow was southerly at the beginning of the period of study and shifted to westerly by the last day of the simulations. This case does not involve strong large-scale forcing as in case 1, but the atmosphere was in general much more humid than in case 2, and conditions were favorable to the development of scattered cumulonimbus clouds. Fog and some strong localized rainfall were present in the region of interest during this period (not shown).

b. Physical parameterizations of PBL processes

Land use and land cover highly influence the spatial variability of surface fluxes in mountainous headwater catchments (Tao and Barros 2013; Flerchinger et al. 2010), where the complexity of the terrain also influences the vegetation distribution. Additionally, mountainous terrain frequently exhibits high spatial variability in the lapse rate on seasonal and daily time scales based on terrain configuration and solar illumination, which has a significant impact on the surface water and energy budgets (Tao and Barros 2017, 2014, 2013; Minder et al. 2010). Jimenez and Dudhia (2012) report that WRF PBL winds are overestimated in valleys/plains and underestimated at high elevations, thus resulting in weaker transport gradients and the underestimation of surface fluxes. Stability conditions, PBL height, surface fluxes, and low-level thermodynamic states and fluxes calculated by different parameterizations of PBL processes interact to determine the spatiotemporal distribution of LLCF.

As higher-resolution simulations (<4 km) become more computationally feasible, discussion has been ongoing in the literature regarding the scale transition between parameterized and explicit physics. Hong and Dudhia (2012) concluded that at least in the case of the planetary boundary layer, the existing parameterizations work well for grid spacing down to approximately 300–500 m. Three different PBL schemes were selected for sensitivity analysis here: the Mellor–Yamada–Janjić (MYJ; Janjić 1994), the Yonsei University (YSU; Hong et al. 2006), and the Mellor–Yamada–Nakanishi–Niino (MYNN, level 2.5; Nakanishi and Niino 2006). The first two (MYJ and YSU) are widely used and have been widely tested, and the third scheme (MYNN) was explicitly designed to improve known problems with the MYJ (although not in complex terrain). A brief description is provided next, and a summary of model simulations is given in Table 2.

The MYJ (Janjić 1994) is a local closure scheme of order 1.5. Its closure constants are determined from neutral data, where turbulent energy production and dissipation are balanced. The heat and moisture flux equations have a countergradient term so that countergradient fluxes from large eddies can be represented. The governing equations are not reproduced here (see Mellor and Yamada 1982). However, the prognostic turbulent kinetic energy (TKE) q equation is expressed as follows:

$$\frac{Dq^2}{Dt} - \frac{\partial}{\partial x_k}\left(lqS_q\frac{\partial q^2}{\partial x_k}\right) = 2(P_s + P_b + \varepsilon), \qquad (1)$$

where l is the master length scale, t is time, x_k is a generic direction in Euclidean space (where $k = 1, 2, 3$), S_q is a
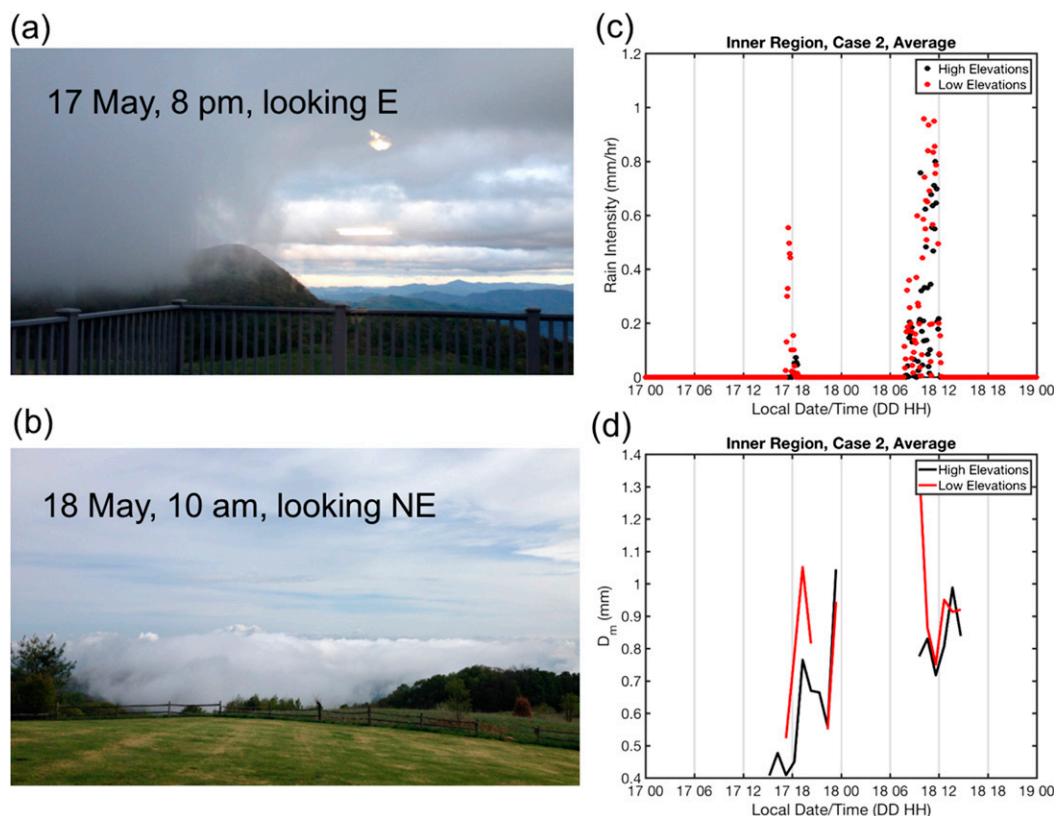
FIG. 4. (a),(b) Photographs taken at station location P3 (Fig. 1b), (c) rain rates observed by PARSIVEL disdrometers in the inner mountain region, and (d) D_m time series observations made by PARSIVEL disdrometers from case 2. Case 2 simulations were run from 0000 UTC 17 May to 0400 UTC 21 May 2014. In (c),(d), colors refer to high/low (black/red) elevations.

dimensionless constant (0.20), P_s is the shear production of turbulent energy term, P_b is the buoyancy production term, and ε is the dissipation. An analysis of the equations in Sun and Barros (2015a) highlights the fact that while the MYJ scheme is classified as "local," meaning that its tendency calculations are dependent upon values only at immediately adjacent heights, it is not strictly so, as it uses an integration throughout the boundary layer to determine the master length scale. Eddy diffusivity in the MYJ is not prescribed, but rather calculated during the simulation, and it depends on the master length scale, turbulent kinetic energy, wind shear, and buoyancy.

The YSU (Hong et al. 2006) parameterization is a nonlocal first-order scheme with explicit entrainment. To compute the turbulent diffusion, nonlocal eddy diffusivity coefficients are used. The equations for all prognostic variables, generically represented by C, are expressed in the form [Eq. (4) from Hong et al. 2006]

TABLE 2. Simulations.

Case	PBL scheme	Surface layer scheme
1: From 0000 UTC 12 May to 0400 UTC 16 May 2014	MYJ	Eta similarity
1: From 0000 UTC 12 May to 0400 UTC 16 May 2014	MYNN	Eta similarity
1: From 0000 UTC 12 May to 0400 UTC 16 May 2014	YSU	MM5 similarity
2: From 0000 UTC 17 May to 0400 UTC 21 May 2014	MYJ	Eta similarity
2: From 0000 UTC 17 May to 0400 UTC 21 May 2014	MYNN	Eta similarity
2: From 0000 UTC 17 May to 0400 UTC 21 May 2014	YSU	MM5 similarity
3: From 0000 UTC 30 May to 0400 UTC 6 Jun 2014	MYJ	Eta similarity
3: From 0000 UTC 30 May to 0400 UTC 6 Jun 2014	MYNN	Eta similarity
3: From 0000 UTC 30 May to 0400 UTC 6 Jun 2014	YSU	MM5 similarity

$$\frac{\partial C}{\partial t} = \frac{\partial}{\partial z}\left[K_c\left(\frac{\partial C}{\partial z} - \gamma_c\right) - \overline{(w'c')}_h\left(\frac{z}{h}\right)^3\right], \qquad (2)$$

where K_c is the eddy diffusivity coefficient, h is the PBL height, C is the prognostic variable placeholder, $(w'c')_h$ is the flux at the inversion layer, z is the height above ground, and γ_c is the countergradient term. The last term on the right side is the flux at the inversion layer including an asymptotic entrainment flux. A parabolic profile is used to prescribe the eddy diffusivity with maximum and mean values proportional to h.

The MYNN, level 2.5 (Nakanishi and Niino 2006), parameterization evolved from the MYJ. Specifically, MYNN closure constants are updated using a database of large eddy simulations as reference. Other improvements include explicit representation of total water content and equivalent potential temperature in condensation physics and a new equation for the master mixing length that is a function of three independent length scales (the surface layer, turbulent layer, and buoyancy).

Multiple studies compare the various PBL parameterizations available within WRF. Erlingis and Barros (2014) found that MYJ is much more sensitive to land surface heterogeneities than YSU over the relatively smooth terrain of the southern Great Plains. Elsewhere, moist and cold biases in the MYJ scheme were reported for simulations in regions from the southeast Pacific to Texas to Europe (e.g., Jousse et al. 2016; Hu et al. 2010; García-Díez et al. 2013). However, García-Díez et al. (2013) also found a warm bias in the MYJ during the winter season in Europe. Cohen et al. (2015) tested a total of five different PBL parameterizations and found that low-level lapse rates are often steeper and smaller in YSU than in MYJ and MYNN, and that while all the schemes overestimate mixed layer convective available potential energy, YSU does so the most. At the 1-km resolution of domain 3 used in this study, YSU performs the best at resolving transport; however, MYNN can show superior results with higher vertical resolution (Shin and Dudhia 2016). Overall, the literature indicates that it is important to carefully consider what is known about the region and the meteorological regime during the period of simulation to construct the optimal model configuration, and that sensitivity tests are often warranted.

While none of the simulations presented here reproduced all aspects of observed LLCF, we found that simulations using MYNN and YSU performed better than MYJ. Rainfall was severely underestimated in MYJ simulations for case 1, and the atmosphere was very dry at low levels during the times of day when fog was most frequently observed in cases 2 and 3 [~1000, ~1800–2000 local time (LT)]. Differences between MYNN and YSU were less marked, although MYNN

performed better in reproducing LLCF formation consistently both at low and high elevations and associated microphysical properties (i.e., higher D_m values at low elevations). LLCF differences were greater among simulations using different microphysical parameterizations tested in WB15 than found among the simulations using the three PBL schemes here.

The primary purpose of the simulations in this study is to provide an interpretative basis for understanding observed LLCF processes. Specifically, the simulations aim to investigate: 1) the spatial distribution and vertical structure of clouds and microphysics represented by the model; 2) the relative contribution of evapotranspiration to the moisture budget for different synoptic forcing conditions; and 3) interactions between local and large-scale dynamics, in particular orographic decoupling and the diurnal cycle of moist processes. Spatial organization along altitudinal gradients at the scale that the model can resolve ($>6\Delta x$), such as larger ridges and valleys, will be discussed in these contexts.

c. Sensitivity analysis of surface and boundary layer processes

Figures 5a–f show Hovmöller diagrams of three surface energy budget terms (sensible heat, latent heat, and ground heat fluxes) output by the Noah land surface model along cross section $A–A'$ marked in Fig. 2b for case 1 (Figs. 5a–c) and case 3 (Figs. 5d–f). The significant daytime discontinuities in ground, sensible, and latent heat fluxes between 82.7° and 82.4°W can be attributed to a change in MODIS vegetation type category from forest to urban corresponding to the city of Asheville metropolitan area. This highlights potential sources of uncertainty in the simulated surface energy budget linked to land-cover classification: land cover is nearly always classified as "forest" in the PRB, meaning that important small-scale urban environments are neglected. In addition, the specification of model parameters (e.g., surface roughness, albedo, and stomatal conductance) based on a broad "forest" classification fails to capture the distinctive characteristics of cove forests and altitudinal vegetation gradients generally. The strength of the frontal passage is striking in how it alters the surface energy budget terms for case 1, especially in the morning on 15 May (Figs. 5a–c). Differences in PBL dynamics do not affect the surface fluxes, and incoming shortwave radiation is the only apparent significant control of the land surface energy budget in the model simulations. This behavior points to some limitations in the coupling between the land surface model and the surface layer and PBL schemes under strong synoptic forcing conditions.

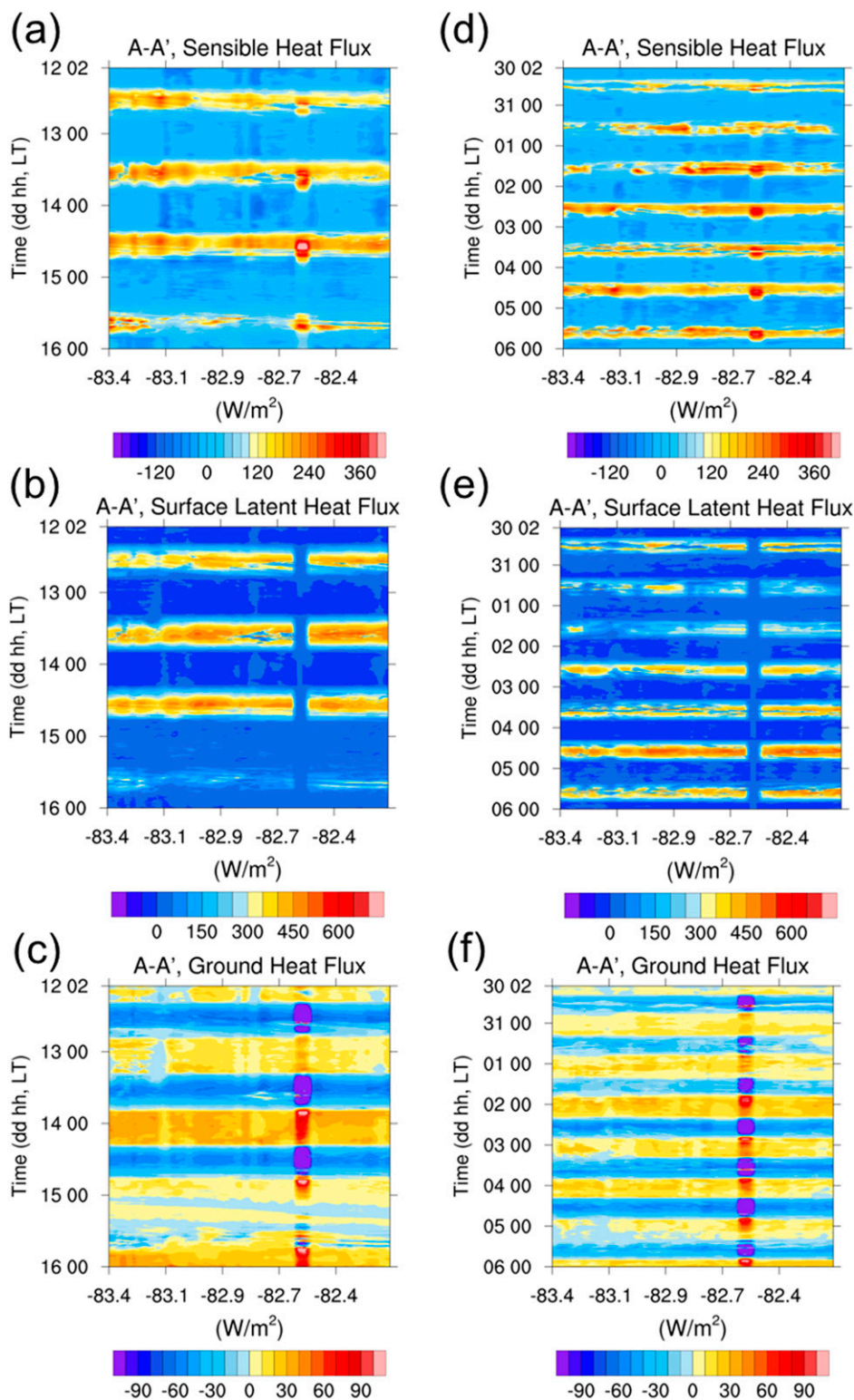An examination of the PBL evolution along with the LCL and cumulative rainfall shows marked differences

FIG. 5. The *A–A'* Hovmöller diagrams of model output (a),(d) sensible; (b),(e) latent; and (c),(f) ground heat flux from case (left) 1 (from 0000 UTC 12 May to 0400 UTC 16 May 2014) and (right) 3 (from 0000 UTC 30 May to 0400 UTC 6 Jun 2014). See Fig. 2b for *A–A'* cross-sectional location. The *x* axis is longitude. Both cases had 6-h spinup. The entire simulation results are plotted here.
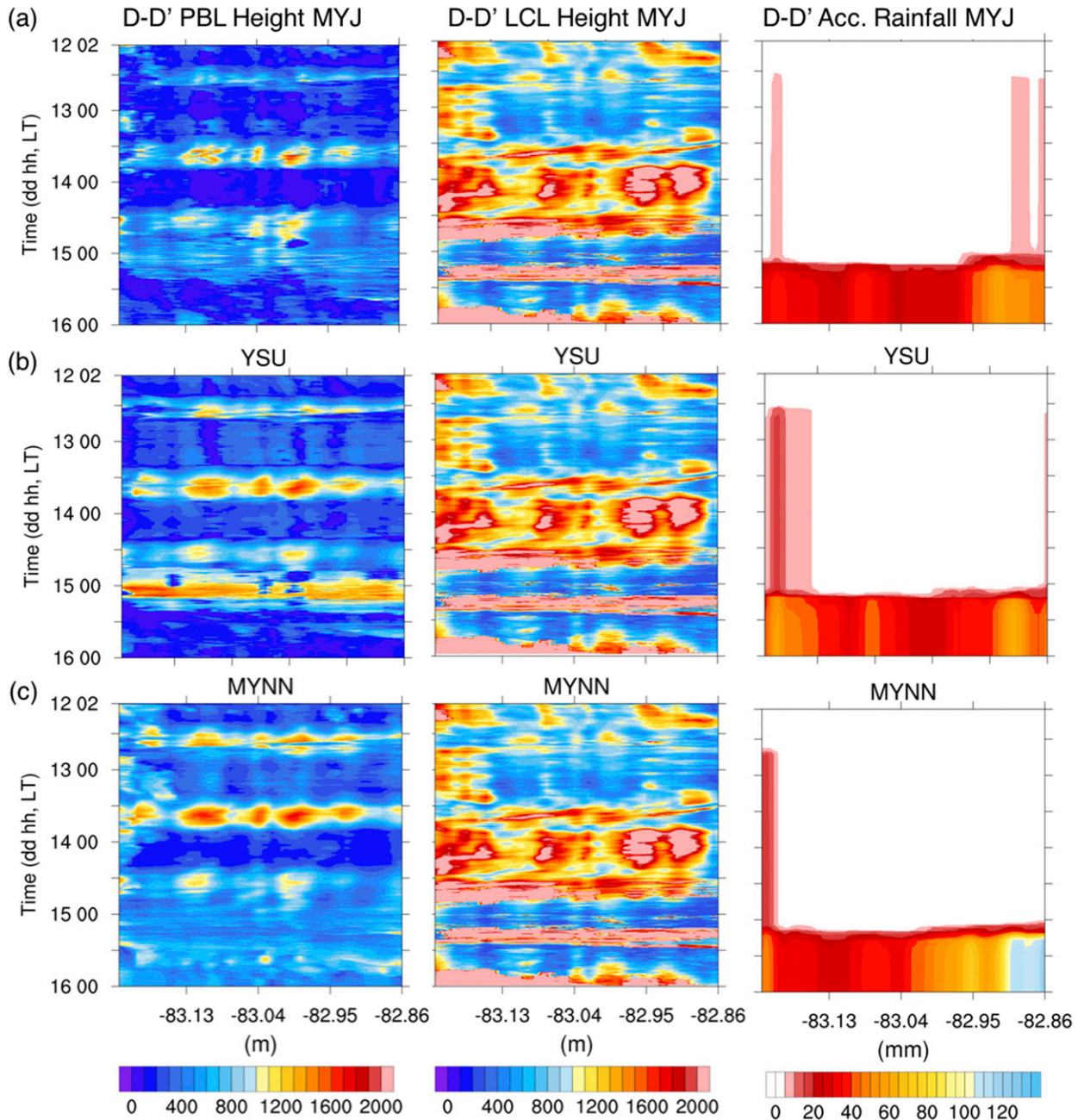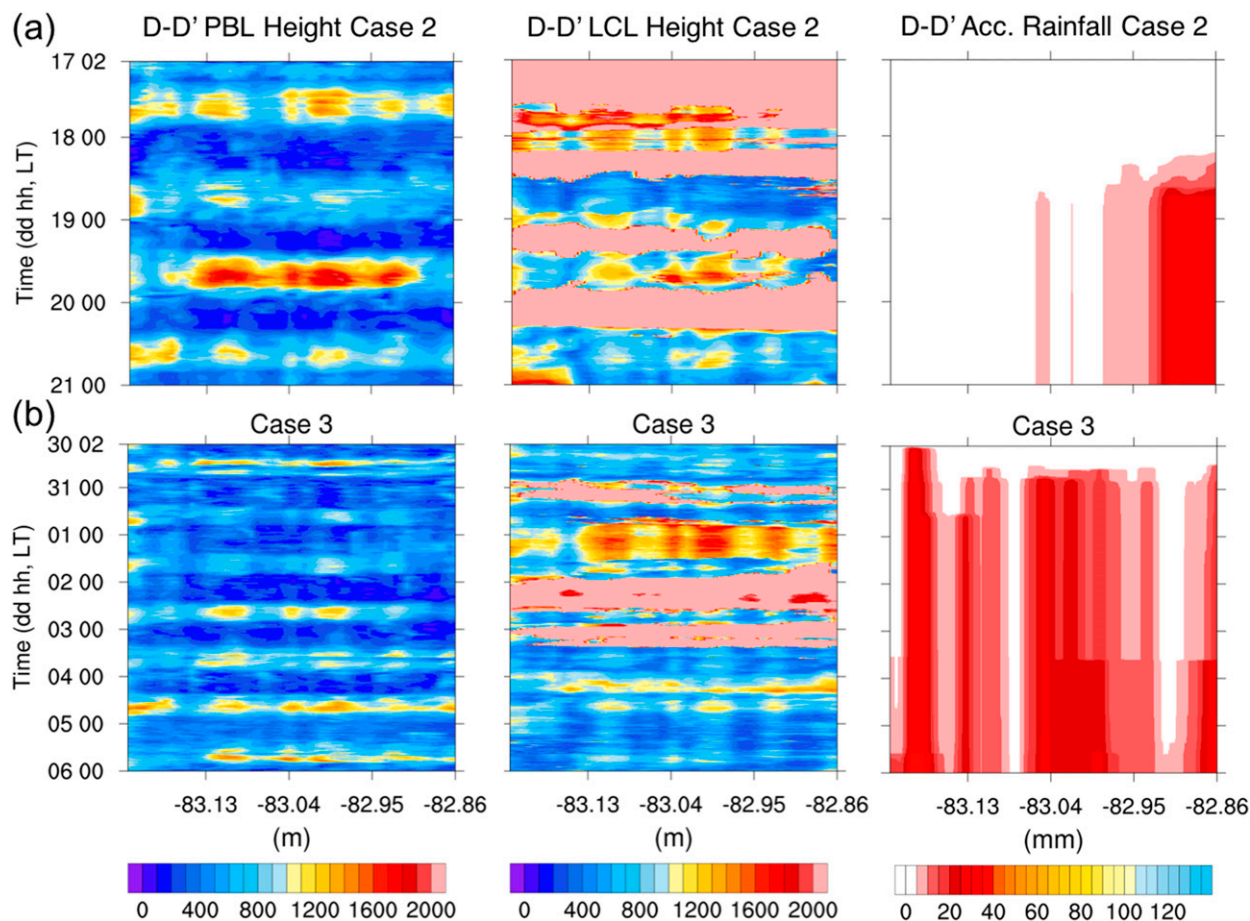
FIG. 6. The D–D' Hovmöller diagrams of (left) PBL height, (center) LCL, and (right) cumulative rainfall for case 1 using each of the different PBL schemes: (a) MYJ, (b) YSU, and (c) MYNN. See Fig. 2b for D–D' cross-sectional location. The x axis is longitude. The entire simulation results are plotted here.

in the PBL heights calculated for the different parameterizations, as expected since the calculation is different between each of the schemes. The YSU scheme uses the bulk Richardson number to identify the first neutral level used as first guess for the PBL height, and the PBL height is adjusted based on the level where the entrainment flux terms of heat, moisture, and momentum are at a minimum. The MYJ identifies the PBL height

based on a threshold of the prognostic TKE (TKE$_{th}$ = $0.1 \, m^2 \, s^2$; Janjić 2002). The MYNN uses the prognostic TKE threshold method when the boundary layer is stable (under 400 m) and a method based on potential temperature fluctuations when the boundary layer is not stable. Specifically, the latter searches for the level at which the potential temperature is over 1.5 K greater than the minimum potential temperature inside the

FIG. 7. The D–D' Hovmöller diagrams of (left) PBL height, (center) LCL, and (right) cumulative rainfall for case (a) 2 and (b) 3 using the MYNN PBL scheme. See Fig. 2b for D–D' cross-sectional location. The x axis is longitude. The entire simulation results are plotted here.

initial calculation of the boundary layer. Among the three schemes, MYNN usually developed the deepest PBL and MYJ the shallowest. Because the PBL height is used in other calculations including other physical parameterizations in WRF, the PBL height differences can contribute potentially to the large differences in accumulated rainfall, among other simulated variables.

Assessing the evolution of the PBL height, LCL, and cumulative rainfall in case 1 for the three different PBL schemes across the D–D' transect in the PRB illuminates important differences. As mentioned above, MYJ simulated the shallowest boundary layer, and the MYNN the deepest (Figs. 6a,c). Note the unphysical behavior in the YSU boundary layer from midnight into the early morning on 15 May during the frontal passage, when the PBL height (~1500 m AGL, typical of early afternoon conditions) is unrealistically high for that time of day, whereas the LCL is realistically at or below 500 m AGL (Fig. 6b). This begs the question of whether the PBL height calculation in YSU, particularly the reliance on the bulk

Richardson number to determine the first neutral level under strong low-level shear conditions, is suitable for complex terrain, at least at 1-km grid spacing.

Figure 6 also illustrates the difference in rainfall magnitudes and spatial patterns among the three schemes. Figure 6 (right) shows rainfall accumulations throughout the simulations. Color changes signify that the model simulated rain at that location along the cross section. The timing is about the same in each simulation with delayed onset (front arrival time) compared to the observations (see WB15 for details). Simulations with the MYNN scheme exhibit the strongest rainfall intensities during the frontal passage. MYJ and YSU underestimate the total cumulative rainfall. YSU and MYNN both reproduced some of the observed vertical structure of clouds and rainfall in the inner mountain region better than MYJ (primarily in the presence and higher concentrations of hydrometeors at low levels). Because of the PBL height inconsistency discussed above, and because the maximum D_m values (e.g., 1.5 vs 1.0 mm in case 1) and hydrometeor
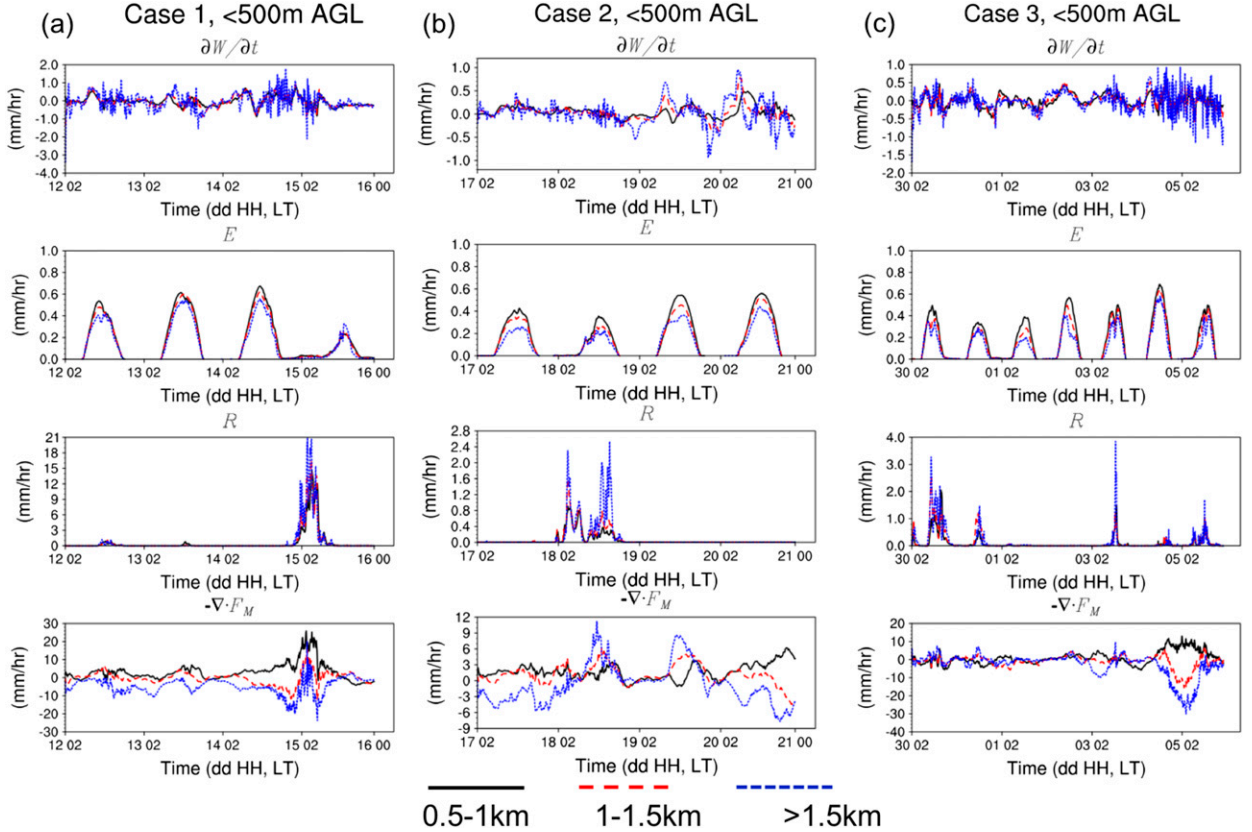
FIG. 8. Moisture budget terms averaged over the PRB for case (a) 1, (b) 2, and (c) 3, where the precipitable water tendency ($\partial W/\partial t$) and the moisture convergence ($-\nabla \cdot F_M$) are integrated below 500 m AGL only. The black, red, and blue lines correspond to terrain masked grid points 0.5–1 (black), 1–1.5 (red), and >1.5 km (blue). Note differences in y-axis scales among left, center, and right plots. The entire simulation results are plotted here.

concentrations near the surface are higher and closer to the observations when the MYNN PBL scheme is used, the latter, more realistic simulations are the focus in the remainder of this study.

The evolution of the PBL height, LCL, and rainfall using MYNN results is shown in Figs. 7a and 7b for cases 2 and 3, respectively. On rain-free days, there are clear patterns in PBL height for both cases, associated with transect D–D′ path across ridgelines on the west side of the PRB (Fig. 2b). The LCL is presented with the same scale as the PBL height for easy identification of times when the LCL is less than or equal to the PBL height. The solid pink color is shown when the LCL is higher than 2 km AGL, and there is a much stronger diurnal cycle shown in the drier case (case 2, Fig. 7a). The PBL height is frequently above or equal to the height of the LCL, in particular during case 3 (Fig. 7b), and at specific locations along the cross sections, thus modulated by the terrain where there are higher PBL heights over the valleys (see Fig. 2c for a profile of the terrain along D–D′).

4. Space–time characteristics of low-level cloud processes

a. Moisture budget

The roles of moisture convergence and evapotranspiration on the diurnal cycle of atmospheric moisture availability in the inner SAM can be isolated by tracking separately the corresponding terms in the moisture budget equation:

$$\frac{\partial W}{\partial t} = E - \nabla \cdot F_M - R, \qquad (3)$$

where the left side represents the temporal evolution of precipitable water W over the column and, on the right-hand side, the first term is the contribution from terrestrial evapotranspiration E, the second term represents moisture divergence ($\nabla \cdot F_M$) calculated from model output, and the third term is rainfall R. The vertical integration is computed based on beta factors (Trenberth 1991). To assess the model's representation of LLC processes along altitudinal gradients, the moisture budget is examined with special attention to

differences in precipitable water tendency and moisture convergence ($-\nabla \cdot F_M$) at different heights in the lower troposphere. Grid points in and around the PRB were stratified into three elevation categories: 500–1000 m (black), 1000–1500 m (red), and greater than 1500 m (blue). These categories correspond to 2675, 1606, and 235 grid points, respectively, in the inner SAM. Figures 8a–c (corresponding to cases 1–3) show moisture budget terms integrated over the lower 500 m. Averages were calculated for all grid points for each elevation class within the PRB. The scale differences in the vertical axis between columns reflect the differences in rainfall and moisture convergence among the three cases. The basin-averaged rainfall is one order of magnitude higher in case 1 than in the others, and the precipitable water tendency is twice as large. Moisture convergence in case 2 is half of the other two cases. Note the decrease in evapotranspiration with elevation in cases 2 and 3 for weak synoptic forcing and weak winds at high elevations consistent with decreases in soil moisture for shallower soils and reduced incoming shortwave radiation due to the presence of clouds. In the aftermath of the frontal passage in case 1, evapotranspiration is uniform across the PRB since soil moisture is near saturation everywhere and therefore not a limiting factor. Clouds are also well distributed.

Moisture convergence patterns change dramatically with gridpoint elevation. In all cases, there is stronger low-level convergence (up to 1.5 km elevation, red and black, Fig. 8) and upper-level divergence (blue, Fig. 8). In case 2, the strongest peaks in both convergence and divergence occur in the afternoon at high elevation. This also happens in cases 1 and 3 on the dry days—note the divergence peaks in 12 and 13 May (Fig. 8a). Large convergence values at the higher-elevation grid points correspond to small-scale rainfall features in case 3. Thus, in days with weak synoptic forcing, ridge clouds form and precipitation results from sustained mesoscale advection of low-level moisture.

The precipitable water tendency and the moisture convergence were integrated vertically up to 2 km AGL to contrast the behavior between upper and lower levels. Precipitable water (not shown) was similar to the 500-m integration. The results for moisture convergence show that in all simulations the differences in the diurnal cycle by elevation class are no longer visible (Fig. 9). That is, the terrain elevation has less of an effect when a deeper atmospheric column that rises well above the envelope orography is considered. The differences are now apparent only for periods of persistent rainfall. This behavior is consistent with the hypothesis of orographic decoupling with terrain controls confined to the lower levels.
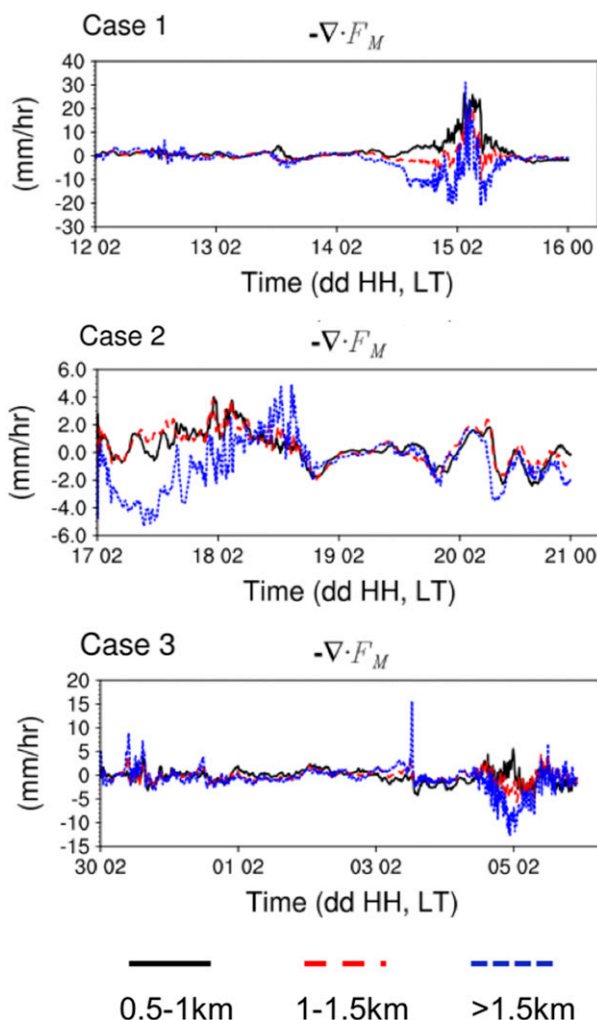

FIG. 9. As in Fig. 8, but for the moisture convergence term ($-\nabla \cdot F_M$) only and integrated within 2 km AGL.

b. Vertical structure of microphysical processes

Microphysical processes are assessed for rainy periods in each simulation. First, D_m is calculated using the two moments (total number concentration N_T and mixing ratio q) provided by the Milbrandt microphysics scheme (Milbrandt and Yau 2005a), and its vertical structure is assessed in the context of the physics that are known for this area. The D_m is necessarily different here than in the calculations shown in WB14 and WB15, as specific information on the exact distribution of the drops is not known. The equation used to compute the mass-weighted mean diameter as output from the model is

$$D_m = \left(\frac{\rho q}{c N_T}\right)^{1/d}, \qquad (4)$$
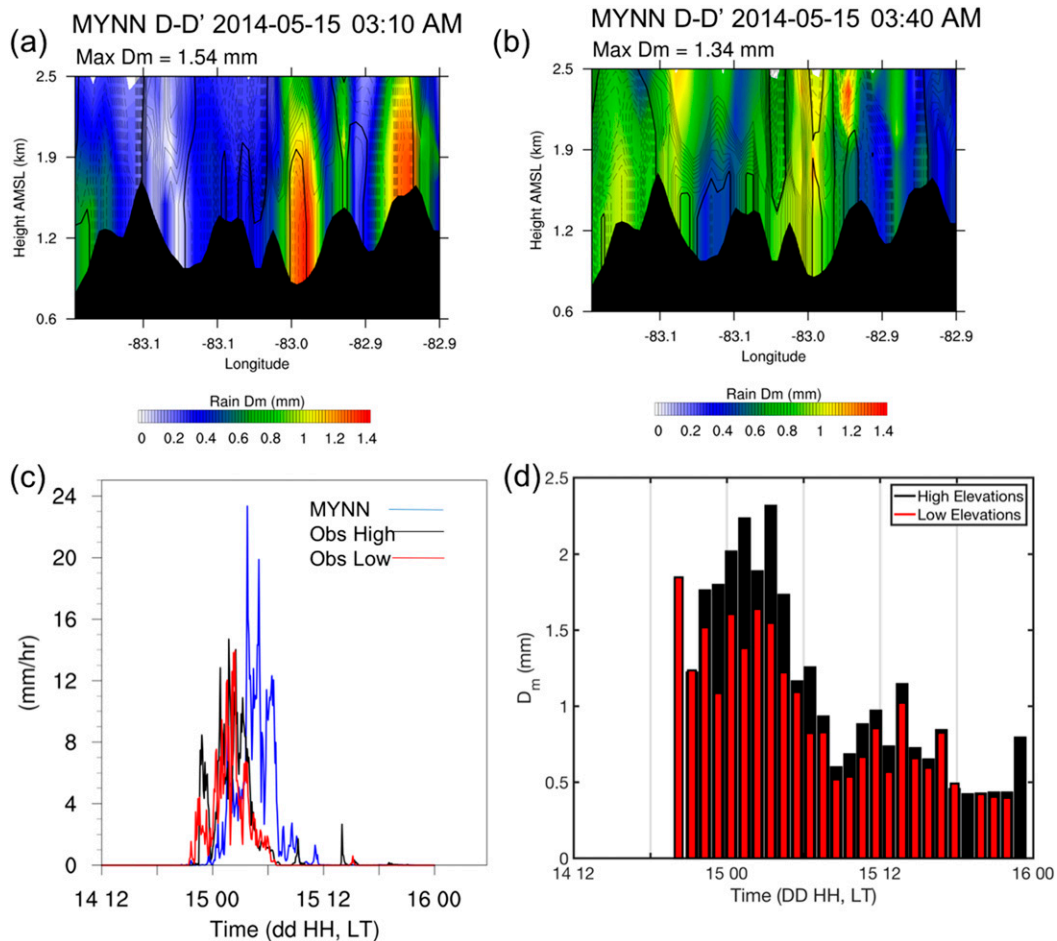
FIG. 10. Vertical profiles of D_m (filled contours) and vertical velocity (contour lines, dashed indicates negative values) over (a),(b) the $D–D'$ cross section, along (c) with the max rainfall at relevant times from the model and inner-region disdrometer observations and (d) D_m as observed by inner-region disdrometers for case 1. Colors in (c) and (d) refer to high/low (black/red) elevations. See Fig. 2b for $D–D'$ cross-sectional location.

where air density ρ is computed using pressure and temperature outputs from WRF, and the coefficients are $c = (\pi/6)10^3$ and $d = 3$.

Figures 10a and 10b show vertical distributions of modeled D_m along $D–D'$ at two times as the front propagated over the PRB during case 1. Figure 10 also shows the maximum rainfall intensity modeled and observed (Fig. 10c) and D_m estimated from DSD observations by the PARSIVEL disdrometers (Fig. 10d), where observations are stratified by elevation: low (valleys and mountain passes) and high (ridgelines). The timing of peak rainfall in the WRF simulations was delayed by 3–4 h, that is, in reality the front arrived in the late evening on 14 May but in the early morning on 15 May in the simulations (see WB15 for a detailed discussion).

In case 1, there are visible patterns of larger D_m approaching 1.5 mm near the ground along with higher number concentrations. This is evidence of hydrometeor

sedimentation, but the D_m profiles predicted are generally uniform in the lower 1 km shown in Fig. 10, which is in contrast with radar profile data (not shown, see WB14) that show stronger increases toward the surface. Further, there is no significant difference between high- and low-elevation D_m statistics in the simulations. The largest values output by the model, with the lowest level at 10 m, approach 2 mm, which is about half of the size reported by the disdrometers for the corresponding stage of the storm.

In case 2, modeled D_m values at the surface are much lower than in case 1. LLCs were observed in case 2, and the values estimated from the surface disdrometer observations, much lower than in case 1, are around 1 mm for this event (Figs. 11a–d). The model overestimates rainfall intensity along $D–D'$ by about 200% at the peak for this event. Storm propagation timing is not an issue in this case as it was in case 1 since synoptic forcing is weak. Differences in the time series of model rainfall
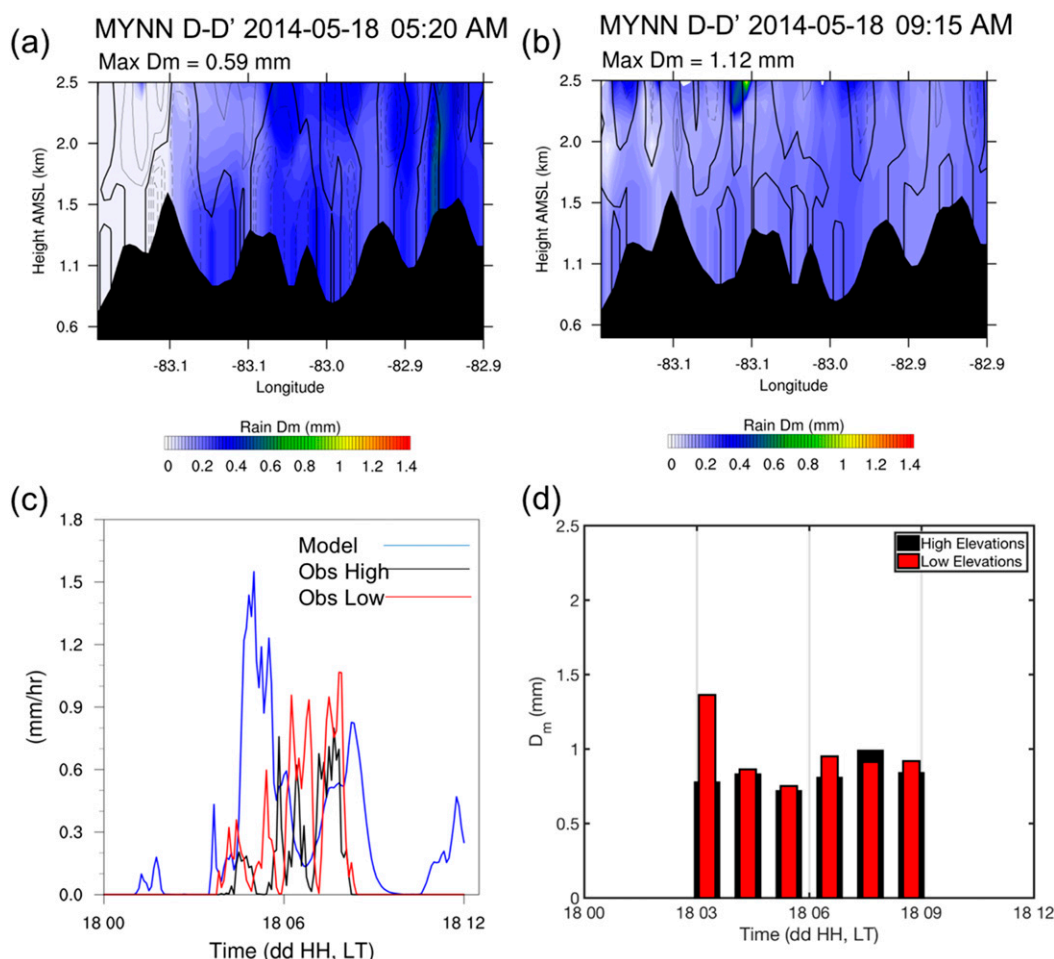
FIG. 11. As in Fig. 10, but for case 3.

(Fig. 11c) in the model are related to the switch from divergence to convergence in the upper levels and increase of low-level convergence (Fig. 8b, bottom; Fig. 9, middle) before 0600 LT 18 May. The lack of vertical cloud structure (Fig. 11b) is consistent with the fact that observed multilayered LLCs did not form in the model simulations. The latter indicates that even higher vertical resolution in the lowest 1 km is likely required.

In case 3 (not shown), the D_m values are much lower. In the western ridges where the rain is heavier because of classical orographic enhancement, and where the model does successfully produce LLC, the contrast and increase in D_m between high and low elevations is close to observations, albeit without significant vertical structure. Thus, when the model captures realistic cloud structure, the microphysical properties are better represented, and vice versa. Elsewhere, and at low elevations in particular, the model does not produce low-level or multilayer clouds. Without these clouds, the enhancement of coalescence processes near the ground is not captured,

resulting in very small D_m values, and thus the reverse orographic enhancement is not simulated. Nevertheless, the space–time organization of clouds and precipitation patterns in the WRF simulations for the different cases shows evidence of the hypothesized governing mechanisms in this region (Fig. 1c) at the meso-γ scale, that is, the model's effective spatial scales [$6\Delta x - 15\Delta x$, where $\Delta x = 1$ km, as per Nogueira and Barros (2014)].

c. Diurnal cycle

Next, the focus is on elucidating the diurnal cycle of moisture convergence on days with weak large-scale forcing. Selected night- (Fig. 12) and daytime (Fig. 13) spatial distributions of low-level winds, evapotranspiration, moisture convergence, temperature, and shortwave radiation for case 1 (13 May 2014) display common features of the diurnal cycle in the PRB for all the simulations and thus can be used toward synthesis of the primary mechanisms driving the local hydrometeorological regimes in the inner SAM.
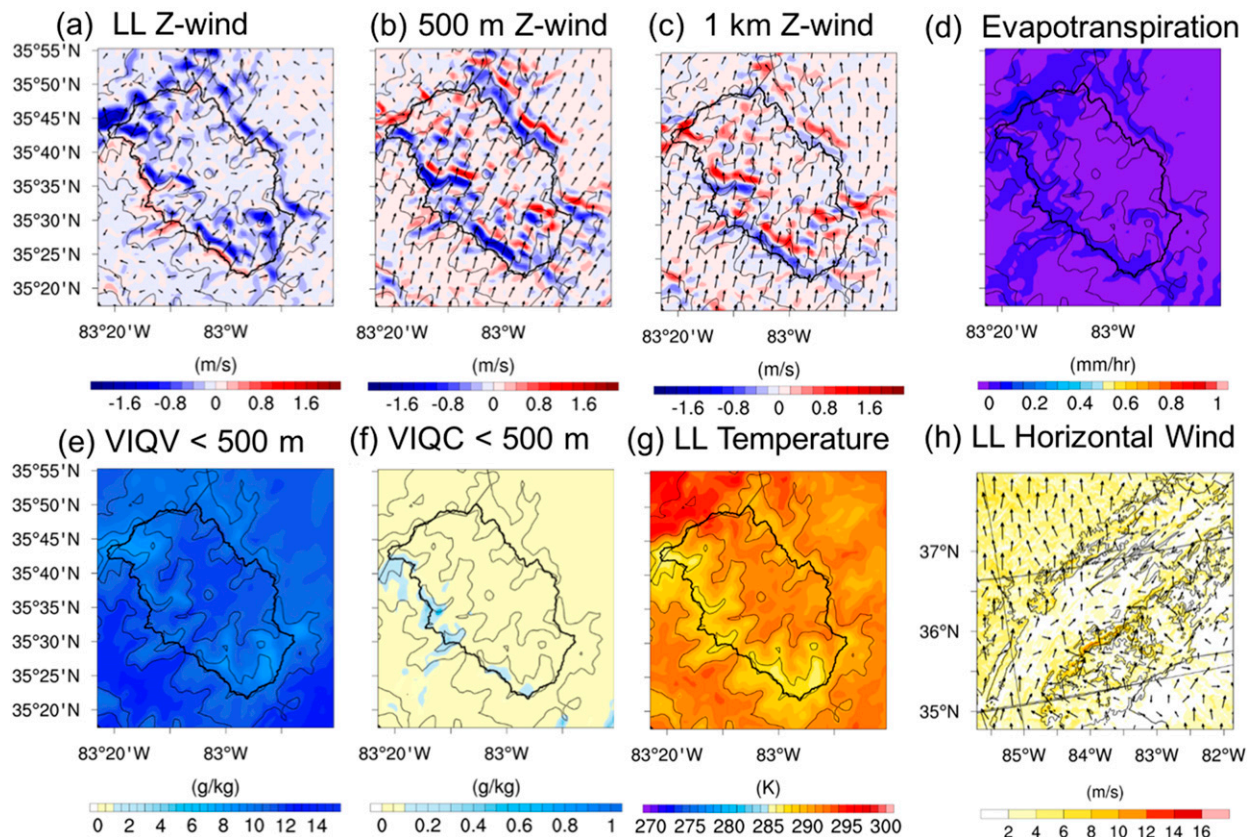
Case 1 -13 May 2014 03:00 LT

FIG. 12. Selected surface and wind variables for case 1 (overnight on 13 May 2014). (a)–(c) Vertical wind (*Z* wind) with horizontal vectors at the lowest model level (LL), 500 m, and 1 km, respectively; (d) evapotranspiration; (e) vertically integrated water vapor (VIQV) below 500 m; (f) vertically integrated cloud water (VIQC) below 500 m; (g) temperature at the LL; and (h) horizontal winds at the LL. The black contour demarks the PRB (see also Fig. 2b). The *x* axis is longitude.

During the night (Figs. 12a–h), very slow horizontal winds and stagnation zones (cold air pools) form at low elevations in the inner region between the west and east topographic divides, and strong sinking motion aligned with the ridges brings mass into the valleys (potentially significant water vapor and aerosol loading—here the flow is southwesterly, coming from upper Tennessee). Note the formation of fog on the Cataloochee Divide (CD; Figs. 1b,c and Fig. 12f) linked to significant surface cooling. Nocturnal radiative cooling trapping the air mass inside the basin enhances cold air accumulation. Once solar forcing begins during the day, the terrain organizes the vertical velocity fields, especially at and above 500 m AGL (about the height of the boundary layer in the early morning), including a shift in the orientation of the vertical waves from west to east at night to southwest to northeast during the day following the sun's trajectory (Figs. 13a–c). Near-surface moisture convergence supports ridge–valley circulations and divergence aloft in the inner region (Figs. 13e,f). On the

western ridges and along the CD, simulations show low temperatures (Fig. 13g) and frequent LLC formation under southerly flow conditions typical of the warm season in the region. Incoming shortwave radiation decreases significantly and evapotranspiration can decrease locally by one order of magnitude in cloudy areas compared to surrounding cloudless areas (Figs. 13d,h). Other days exhibit the same diurnal cycle, showing nocturnal transport of moisture into the basin along the western ridges followed by daytime circulations that transport valley moisture plus contributions from evapotranspiration upslope in the PRB.

Nighttime and daytime vertical velocity contours at two different levels are shown in Fig. 14 (case 2, Figs. 14a,b; case 3, Figs. 14c,d). As in case 1, strong sinking occurs after moisture crosses the ridges at the PRB's southwestern boundary. Higher in the atmosphere, the flow becomes increasingly westerly. The overall flow on this date was southwesterly with a marked decrease in horizontal wind speed in the inner
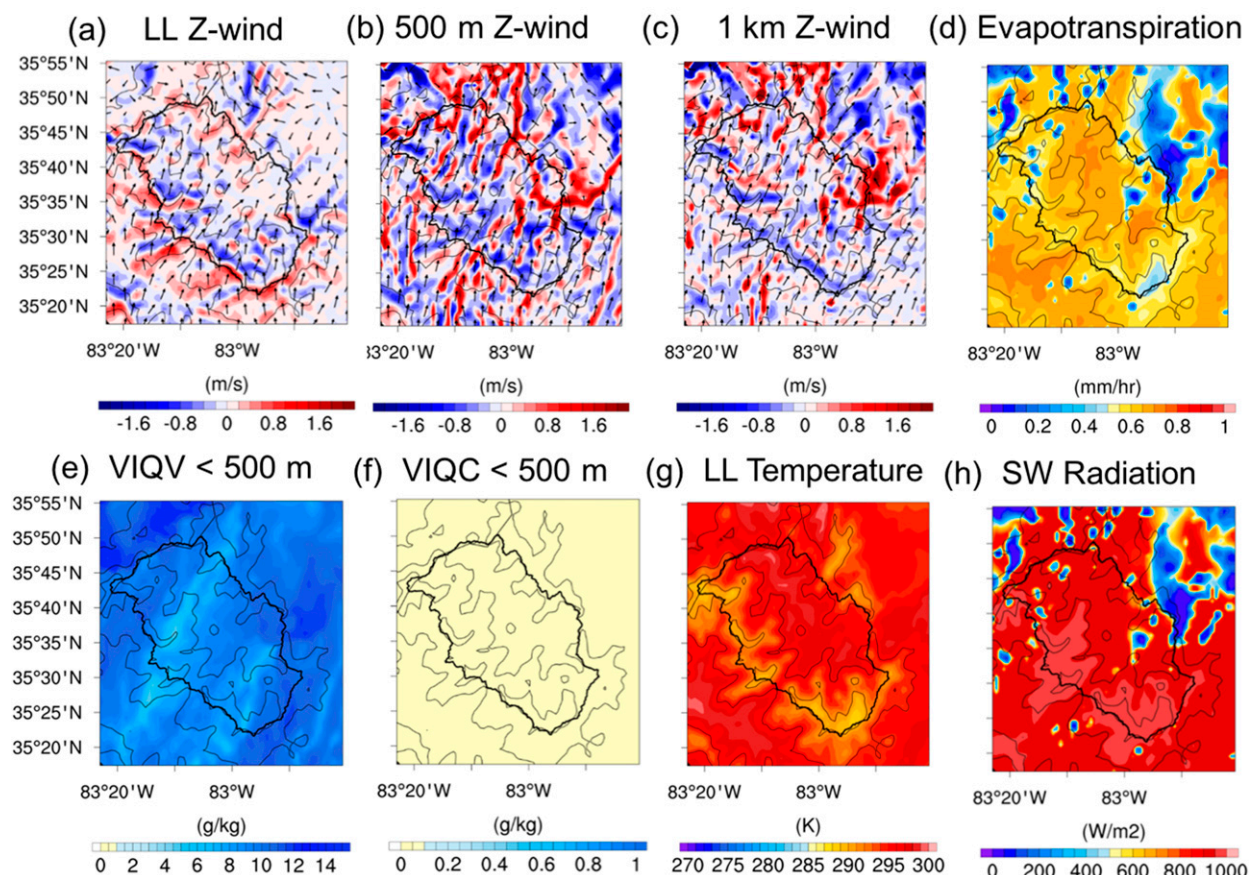
FIG. 13. (a)–(g) As in Fig. 12, but for case 1 (afternoon on 13 May 2014). (h) Shortwave surface radiation values.

SAM, showing the influence of the low-level terrain modulating the flow propagation. In this case, nighttime vertical velocities at 500 m (not shown) and 1000 m already show some organization along the southwestern ridges, which strengthens as the day progresses. This corroborates the description of local flows controlled by the large-scale influence of solar forcing from above and terrain at the surface, organizing the flow patterns into bands perpendicular to the boundary of the basin and along ridgelines crossing the basin.

The pattern on 4 June, a day simulated during case 3, also shows this same overarching pattern with strong sinking motion and mass transport across the southern boundary at low levels (Figs. 14c,d). However, there is strong directional shear between the 500 m (not shown) and 1 km AGL vertical velocities. Overnight, this results in large disorganized areas of weak downdrafts at 1 km. The vertical velocity patterns formed after sunrise on this date are perpendicular to the boundary at the 500-m level but change orientation at the 1-km level with orientation similar to the surface patterns (Fig. 14d) and very different

from case 2 (Fig. 14b). Case 3 was much wetter than case 2, with rainfall-producing cumulonimbus observed during IPHEx and scattered showers throughout the PRB.

In each case, evapotranspiration is at least one order of magnitude lower than moisture convergence, and therefore its contribution to rainfall through recycling is negligible as in the eastern Andes (Sun and Barros 2015a). Like in the Andes, evapotranspiration is a source of low-level instability that, along with solar forcing, plays an important role in the diurnal cycle of the PBL and contributes to the demise of orographic decoupling in the daytime.

Figures 15a–f show the surface vertical velocities, 500-m horizontal winds, and the west–east vertical structure along cross section $I–I'$ of the square of the Froude (Fr) number in the broader SAM region at 0700 UTC (~0300 LT) and 2200 UTC (~1800 LT) 20 May 2014, respectively. The Froude number $[\mathrm{Fr}^2(x, z) = U^2/(z^2 N_m^2)$, where U is the root-mean-square (RMS) of the zonal wind speed, N_m is the moist Brunt–Väisälä frequency, and z is the model level
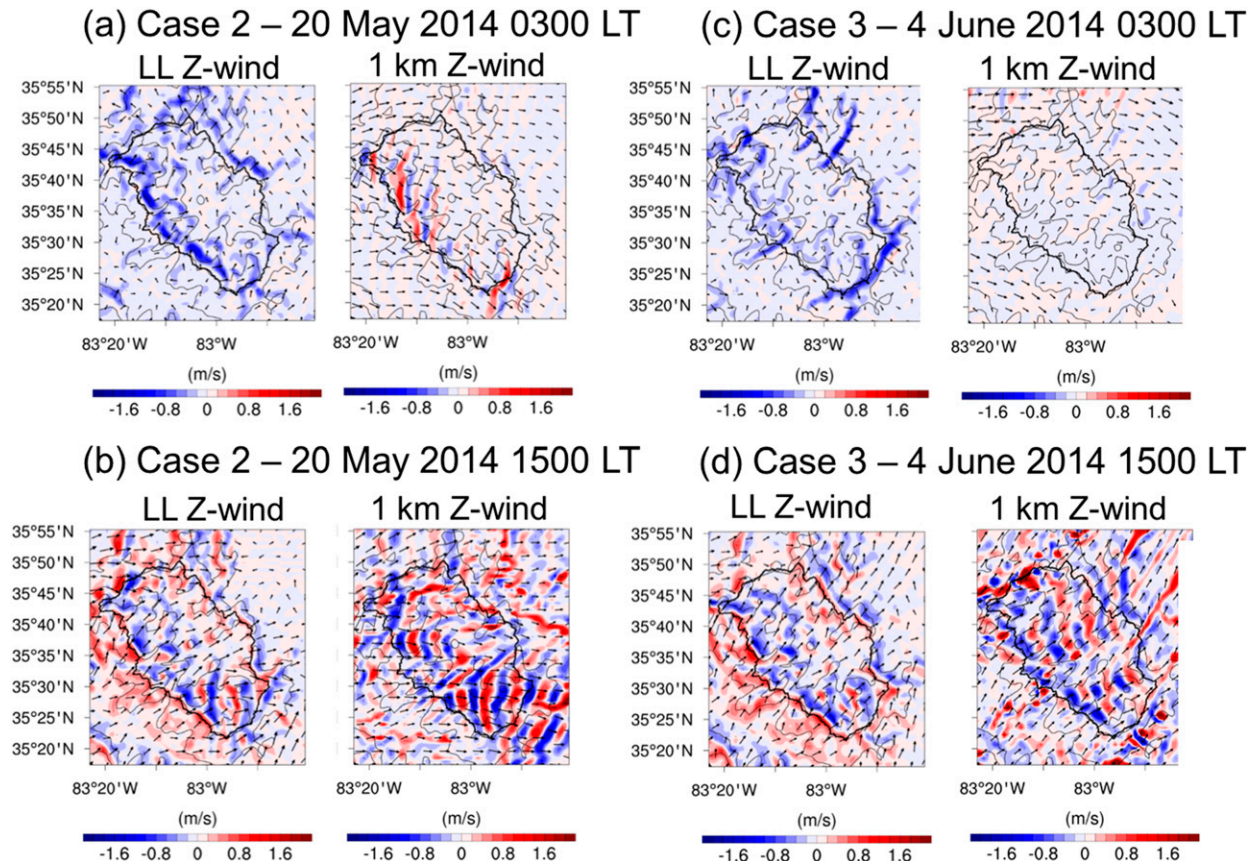
FIG. 14. Vertical wind (Z wind) at the LL and at 1 km at (a),(c) 0300 LT and (b),(d) 1500 LT for (left) case 2 (20 May 2014) and (right) case 3 (4 Jun 2014). The x axis is longitude.

height] compares the zonal kinetic energy with local potential convective energy. Very low Fr^2 values indicate increased local stratification, and values approaching zero indicate the development of a stagnation zone and potential flow separation (Figs. 15c,f). These stagnation zones are important in controlling local circulations, modulate long time-scale development of rain shadows, and affect interactions of fronts and other synoptic-scale patterns with the terrain (Hunt et al. 1997; Smolarkiewicz and Rotunno 1989, 1990; Galewsky 2009). Negative Fr^2 values are indicative of local instability ($N_m^2 < 0$). At night, ubiquitous alignment of strong downdrafts with ridge features at all scales independent of orientation (zonal or latitudinal) is apparent (Fig. 15a). However, there is a strong contrast between the horizontal winds on the valley and ridge and Appalachian Plateaus region to the west and the SAM proper, with marked slowdown and near arrest at and below 500 m AGL in the SAM, consistent with the nighttime cold air pooling and slow horizontal flows in the inner region noted earlier (Fig. 15b). This contrast is well captured by the vertical cross section of Fr^2, with

stable conditions ($N_m^2 > 0$) everywhere except over the western ridges of the SAM, where it approaches near-stagnation conditions at low levels (<500 m), and separation with propagation of internal gravity waves between 500 m and 2 km above is evidence of orographic decoupling (Fig. 15c). During daytime, solar forcing triggers upward motion (Fig. 15d) that results in the formation of vertically propagating waves with strong horizontal flows (Fig. 15e), deeper PBL, and widespread moist instability in the SAM (Fig. 15f). The region of slow flow below the ridgelines contracts from east to west during the day, and low-level easterly advection and ridge–valley circulations redistribute moisture from the valleys to the ridges in the inner region.

Thus, WRF is simulating a diurnal cycle in the PRB that is controlled largely by nighttime stable large-scale transport and leeward downslope flows, and daytime solar forcing, with westerly moisture advection at upper levels, easterly and southeasterly low-level mesoscale moisture advection, and ridge–valley circulations. Temporally, all cases exhibit two distinct modes of orographic controls on atmospheric moisture convergence patterns
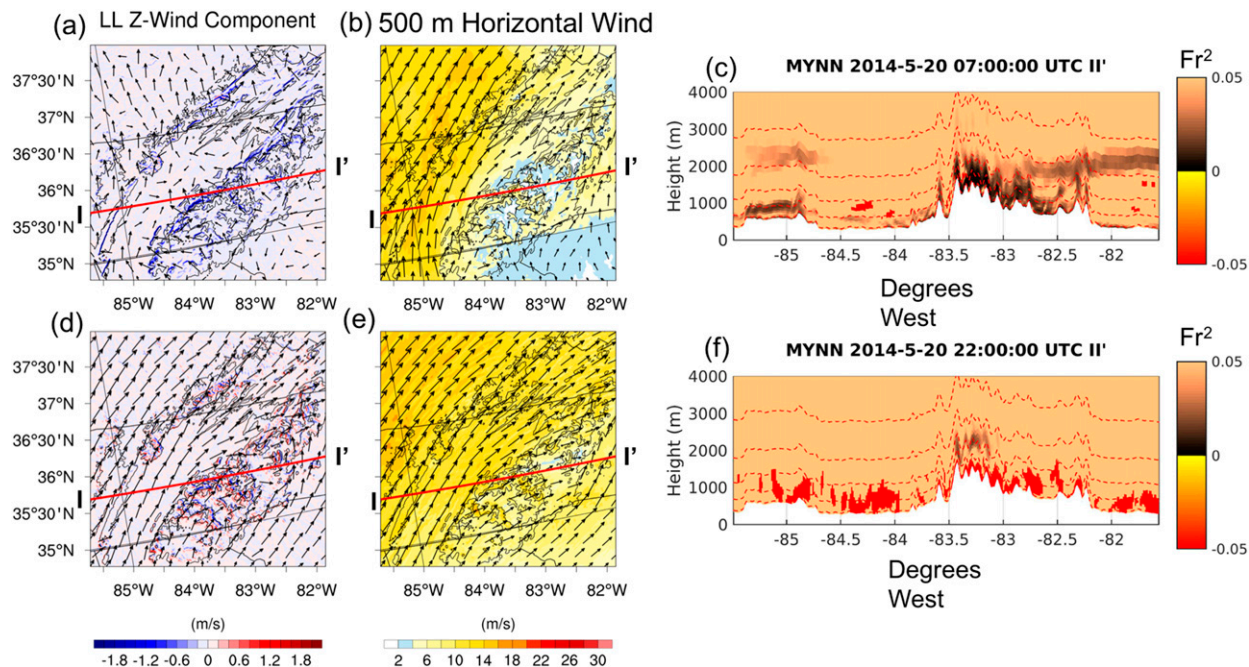
FIG. 15. Case 2 flow characteristics at (a)–(c) 0300 and (d)–(f) 1800 LT: (left) LL vertical wind (Z wind), (center) 500-m AGL horizontal winds, and (right) Fr^2 distributions along cross section $I–I'$. The x axis is longitude.

that explain the diurnal cycle of LLCF at different scales. At night, the simulations show a stationary mode at the meso-α scales associated with an extended flow separation zone that supports low-level pooling and trapping ($Fr^2 \sim 0$) of cold, moist, stable air ($N_m^2 > 0$) in the inner mountain basins on the lee side of the western topographic divide extending to the eastern topographic divide, that is, nocturnal transport of mass into the basin during the night and harboring of that mass until sunrise. During the day, the inner basin is heated, triggering low-level divergence consistent with the coorganization of ridge–valley circulations at the meso-γ scale and Rayleigh–Bénard convection at the meso-β scale characterized by
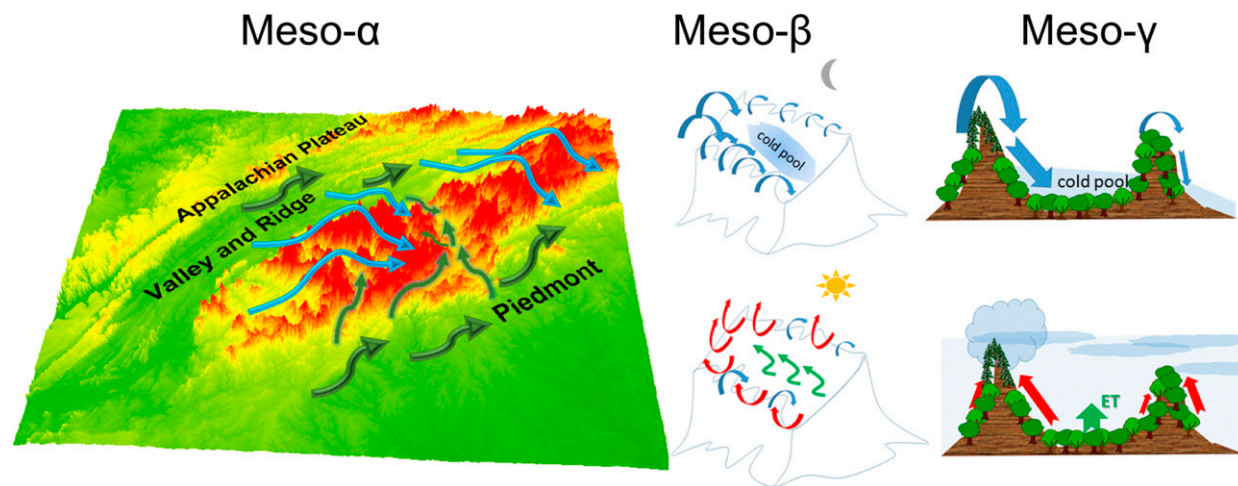
FIG. 16. Diurnal cycle of modeled moisture transport at different mesoscales: meso-α (>200 km) moisture convergence patterns dominated by westerly flows and sinking motion along the western ridges of the SAM (blue arrows) and predominantly easterly valley flows into the inner region (green arrows); meso-β (20–200 km) daytime roll circulations associated with solar forcing organize moisture divergence and convergence along ridges on elevated terrain; and meso-γ (<20 km) daytime ridge–valley circulations in the inner region (downdrafts are in blue and updrafts are in red).

widespread low-level instability ($N_m^2 < 0$) below the envelope orography as the shallow region of slow flow retreats to the western boundary of the inner region ($Fr^2 \sim 0$). Lateral valley–ridge and roll circulations organize the vertical velocity fields around the landform, leading to convective activity in the afternoon with strong vertical motions and patterns of cloud formation strongly correlated with the terrain at low levels (within 500 m of ground level). A conceptual synthesis of the key governing mesoscale mechanisms (meso-α scale, ~200–2000 km; meso-β scale, ~20–200 km; and meso-γ scale, 2–20 km) is depicted in Fig. 16 with the PRB boundary marked.

5. Conclusions and discussion

The simulations conducted illustrate the importance of terrain characteristics on flow patterns, conducive to favorable conditions for formation of low-level convergence and divergence zones that exhibit persistent diurnal cycles independently of large-scale forcing. Topographically forced lifting and low LCL in combination with mass transport into the basin provide the thermodynamic context for the formation of LLCF. LLC are organized via mountain–valley flows after the onset of solar heating when larger-scale moisture transport is weak at low levels, or else limited to higher levels in the atmosphere, as in case 2 (schematic in Fig. 16).

At nighttime, in the absence of large-scale forcing, orographic decoupling determines moisture convergence patterns, trapping cold air at low levels below the envelope topography. During the day, this effect disappears and the low-level circulations are controlled by solar forcing, landform, and moisture availability. Easterly and southeasterly moisture convergence are the dominant pathways of daytime remote moisture advection into the inner region. During periods of lower rainfall and soil moisture in the Piedmont, this remote influx of moisture is considerably lower than for normal conditions, and daytime LLC formation in the inner region significantly decreases as the LCL rises, thus inhibiting daytime rainfall locally in the absence of synoptic forcing. This may explain the west-to-east progression of severe drought in regional climatology.

Care still needs to be taken to ensure accurate representation of land use and land cover in the model, which could provide a very different lower boundary condition to the PBL parameterizations, in both sign and order of magnitude (Fig. 5). While none of the PBL schemes produced the observed vertical structure of LLCF in the inner SAM at all observed times, the MYNN and YSU schemes outperformed MYJ and did a reasonable job given the resolution of land cover here, by reproducing low-level cloud tied to the ridges at the western boundary. In combination with an improved land-use/land-cover dataset such as that created for the terrain, results should be more realistic and appropriate for the investigation of processes at even smaller scales.

In an assessment of the vertical structure of the microphysics, D_m values computed with the model are significantly lower than observed and did not show the expected increase toward the surface along the $D–D'$ cross section in accordance with the observed pre-event presence of LLCF and resulting enhancement of coalescence, but the model reproduced this effect to some degree at the western boundary. This is not unexpected given the model's resolution impact on the spatial patterns of simulated LLCF. If data assimilation runs were made that implemented their placement a priori, using observations from the inner SAM cloud radar and microwave radiometer data available during IPHEx, this is expected to be clearer. However, with this said, the model did not reproduce the vertical microphysical stratification expected during warm rain processes generally, and the representation of these processes in the model needs improvement.

Despite the limits of these model simulations, the impact of low-level processes—evapotranspiration patterns, terrain-driven flow patterns and diurnal cycle, and resulting formation of LLCF—was captured. Conducting simulations at higher resolution and with more realistic land cover will show additional levels of space–time variability, that is, the preferential areas where this moisture converges, along with longer-range transport from locations such as the Gulf of Mexico, the southeast, or the west via fronts and mesoscale convective systems. These areas serve to nourish and sustain richly biodiverse areas like cove forests that thrive on persistent immersion in LLCF.

REFERENCES

Angulo-Martínez, M., and A. P. Barros, 2015: Measurement uncertainty in KE–*I* relationships for soil erosion studies: An evaluation using PARSIVEL disdrometers in the southern Appalachian Mountains. *Geomorphology*, **228**, 28–40, doi:10.1016/j.geomorph.2014.07.036.

Barros, A. P., G. Kim, E. Williams, and S. W. Nesbitt, 2004: Probing orographic controls in the Himalayas during the monsoon using satellite imagery. *Nat. Hazards Earth Syst. Sci.*, **4**, 29–51, doi:10.5194/nhess-4-29-2004.

——, and Coauthors, 2014: NASA GPM-Ground Validation: Integrated Precipitation and Hydrology Experiment 2014 Science Plan. Tech. Rep., Duke University, 64 pp., doi:10.7924/G8CC0XMR.

Bhushan, S., and A. P. Barros, 2007: A numerical study to investigate the relationship between moisture convergence patterns and orography in central Mexico. *J. Hydrometeor.*, **8**, 1264–1284, doi:10.1175/2007JHM791.1.

Bindlish, R., and A. P. Barros, 1996: Aggregation of digital terrain data using a modified fractal interpolation scheme. *Comput. Geosci.*, **22**, 907–917, doi:10.1016/S0098-3004(96)00049-0.

Clark, S. H. B., 2009: Birth of the mountains: The geologic story of the southern Appalachian Mountains. USGS Publ., 26 pp. [Available online at https://pubs.usgs.gov/gip/birth/.]

Cohen, A. E., S. M. Cavallo, M. C. Coniglio, and H. E. Brooks, 2015: A review of planetary boundary layer parameterization schemes and their sensitivity in simulating southeastern U.S. cold season severe weather environments. *Wea. Forecasting*, **30**, 591–612, doi:10.1175/WAF-D-14-00105.1.

Daly, C., D. R. Conklin, and M. H. Unsworth, 2010: Local atmospheric decoupling in complex topography alters climate change impacts. *Int. J. Climatol.*, **30**, 1857–1864, doi:10.1002/joc.2007.

DellaSala, D. A., P. Alaback, T. Spribille, H. von Wehrden, and R. S. Nauman, 2011: Just what are temperate and boreal rainforests? *Temperate and Boreal Rainforests of the World: Ecology and Conservation*, D. A. DellaSala, Ed., Island Press, 1–41, doi:10.5822/978-1-61091-008-8_1.

Dollison, R. M., 2010: The National Map: New viewer, services, and data download. USGS Fact Sheet 2010-3055, 2 pp. [Available online at https://pubs.er.usgs.gov/publication/fs20103055.]

Duan, Y., A. Wilson, and A. P. Barros, 2015: Scoping a field experiment: Error diagnostics of TRMM Precipitation Radar estimates in complex terrain as a basis for IPHEX2014. *Hydrol. Earth Syst. Sci.*, **19**, 1501–1520, doi:10.5194/hess-19-1501-2015.

Dudhia, J., 1989: Numerical study of convection observed during the Winter Monsoon Experiment using a mesoscale two-dimensional model. *J. Atmos. Sci.*, **46**, 3077–3107, doi:10.1175/1520-0469(1989)046<3077:NSOCOD>2.0.CO;2.

Dyer, J. M., 2009: Assessing topographic patterns in moisture use and stress using a water balance approach. *Landsc. Ecol.*, **24**, 391–403, doi:10.1007/s10980-008-9316-6.

Ek, M. B., K. E. Mitchell, Y. Lin, E. Rogers, P. Grunmann, V. Koren, G. Gayno, and J. D. Tarpley, 2003: Implementation of Noah land surface model advances in the National Centers for Environmental Prediction operational mesoscale Eta Model. *J. Geophys. Res.*, **108**, 8851, doi:10.1029/2002JD003296.

Erlingis, J. M., and A. P. Barros, 2014: A study of the role of daytime land–atmosphere interactions on nocturnal convective activity in the southern Great Plains during CLASIC. *J. Hydrometeor.*, **15**, 1932–1953, doi:10.1175/JHM-D-14-0016.1.

Flerchinger, G. N., D. Marks, M. L. Reba, Q. Yu, and M. S. Seyfried, 2010: Surface fluxes and water balance of spatially varying vegetation within a small mountainous headwater catchment. *Hydrol. Earth Syst. Sci.*, **14**, 965–978, doi:10.5194/hess-14-965-2010.

Galewsky, J., 2009: Rain shadow development during the growth of mountain ranges: An atmospheric dynamics perspective. *J. Geophys. Res.*, **114**, F01018, doi:10.1029/2008JF001085.

García-Díez, M., J. Fernández, L. Fita, and C. Yagüe, 2013: Seasonal dependence of WRF Model biases and sensitivity to PBL schemes over Europe. *Quart. J. Roy. Meteor. Soc.*, **139**, 501–514, doi:10.1002/qj.1976.

Giovannettone, J. P., and A. P. Barros, 2008: A remote sensing survey of the role of landform on the organization of orographic precipitation in central and southern Mexico. *J. Hydrometeor.*, **9**, 1267–1283, doi:10.1175/2008JHM947.1.

——, and ——, 2009: Probing regional orographic controls of precipitation and cloudiness in the central Andes using satellite data. *J. Hydrometeor.*, **10**, 167–182, doi:10.1175/2008JHM973.1.

Hong, S.-Y., and J. Dudhia, 2012: Next-generation numerical weather prediction: Bridging parameterization, explicit clouds, and large eddies. *Bull. Amer. Meteor. Soc.*, **93**, ES6–ES9, doi:10.1175/2011BAMS3224.1.

——, Y. Noh, and J. Dudhia, 2006: A new vertical diffusion package with an explicit treatment of entrainment processes. *Mon. Wea. Rev.*, **134**, 2318–2341, doi:10.1175/MWR3199.1.

Hou, A. Y., and Coauthors, 2014: The Global Precipitation Measurement mission. *Bull. Amer. Meteor. Soc.*, **95**, 701–722, doi:10.1175/BAMS-D-13-00164.1.

Hu, X.-M., J. W. Nielsen-Gammon, and F. Zhang, 2010: Evaluation of three planetary boundary layer schemes in the WRF Model. *J. Appl. Meteor. Climatol.*, **49**, 1831–1844, doi:10.1175/2010JAMC2432.1.

Hunt, J. C. R., Y. Feng, P. F. Linden, M. D. Greenslade, and S. D. Mobbs, 1997: Low-Froude-number stable flows past mountains. *Nuovo Cimento*, **20**, 261–272.

Janjić, Z. I., 1994: The step-mountain eta coordinate model: Further developments of the convection, viscous sublayer, and turbulence closure schemes. *Mon. Wea. Rev.*, **122**, 927–945, doi:10.1175/1520-0493(1994)122<0927:TSMECM>2.0.CO;2.

——, 2002: Nonsingular implementation of the Mellor–Yamada level 2.5 scheme in the NCEP Meso model. NCEP Office Note 437, 61 pp. [Available online at http://www.emc.ncep.noaa.gov/officenotes/newernotes/on437.pdf.]

Jimenez, P. A., and J. Dudhia, 2012: Improving the representation of resolved and unresolved topographic effects on surface wind in the WRF Model. *J. Appl. Meteor. Climatol.*, **51**, 300–316, doi:10.1175/JAMC-D-11-084.1.

Jousse, A., A. Hall, F. Sun, and J. Teixeira, 2016: Causes of WRF surface energy fluxes biases in a stratocumulus region. *Climate Dyn.*, **46**, 571–584, doi:10.1007/s00382-015-2599-9.

Kain, J. S., 2004: The Kain–Fritsch convective parameterization: An update. *J. Appl. Meteor.*, **43**, 170–181, doi:10.1175/1520-0450(2004)043<0170:TKCPAU>2.0.CO;2.

Kalnay, E., and Coauthors, 1996: The NCEP/NCAR 40-Year Reanalysis Project. *Bull. Amer. Meteor. Soc.*, **77**, 437–471, doi:10.1175/1520-0477(1996)077<0437:TNYRP>2.0.CO;2.

Mellor, G. L., and T. Yamada, 1982: Development of a turbulence closure model for geophysical fluid problems. *Rev. Geophys. Space Phys.*, **20**, 851–875, doi:10.1029/RG020i004p00851.

Milbrandt, J. A., and M. K. Yau, 2005a: A multimoment bulk microphysics parameterization. Part I: Analysis of the role of the

spectral shape parameter. *J. Atmos. Sci.*, **62**, 3051–3064, doi:10.1175/JAS3534.1.

——, and ——, 2005b: A multimoment bulk microphysics parameterization. Part II: A proposed three-moment closure and scheme description. *J. Atmos. Sci.*, **62**, 3065–3081, doi:10.1175/JAS3535.1.

Minder, J. R., P. W. Mote, and J. D. Lundquist, 2010: Surface temperature lapse rates over complex terrain: Lessons from the Cascade Mountains. *J. Geophys. Res.*, **115**, D14122, doi:10.1029/2009JD013493.

Mlawer, E. J., S. J. Taubman, P. D. Brown, M. J. Iacono, and S. A. Clough, 1997: Radiative transfer for inhomogeneous atmospheres: RRTM, a validated correlated-*k* model for the longwave. *J. Geophys. Res.*, **102**, 16 663–16 682, doi:10.1029/97JD00237.

Nakanishi, M., and H. Niino, 2006: An improved Mellor–Yamada level 3 model: Its numerical stability and application to a regional prediction of advecting fog. *Bound.-Layer Meteor.*, **119**, 397–407, doi:10.1007/s10546-005-9030-8.

NCAR, 2012: Yellowstone: IBM iDataPlex System (NCAR Community Computing). NCAR Computational and Information Systems Lab, accessed 4 April 2017. [Available online at http://n2t.net/ark:/85065/d7wd3xhc.]

Nogueira, M., and A. P. Barros, 2014: The nonconvective/convective structural transition in stochastic scaling of atmospheric fields. *J. Geophys. Res. Atmos.*, **119**, 13 771–13 794, doi:10.1002/2014JD022548.

Oke, T. R., 1978: *Boundary Layer Climates.* 2nd ed. Routledge, 435 pp.

Prat, O. P., and A. P. Barros, 2010: Ground observations to characterize the spatial gradients and vertical structure of orographic precipitation—Experiments in the inner region of the Great Smoky Mountains. *J. Hydrol.*, **391**, 141–156, doi:10.1016/j.jhydrol.2010.07.013.

Reinhardt, K., and W. K. Smith, 2008: Impacts of cloud immersion on microclimate, photosynthesis and water relations of *Abies fraseri* (Pursh.) Poiret in a temperate mountain cloud forest. *Oecologia*, **158**, 229–238, doi:10.1007/s00442-008-1128-5.

Shanks, R. E., 1954: Climates of the Great Smoky Mountains. *Ecology*, **35**, 354–361, doi:10.2307/1930098.

Shin, H. H., and J. Dudhia, 2016: Evaluation of PBL parameterizations in WRF at subkilometer grid spacings: Turbulence statistics in the dry convective boundary layer. *Mon. Wea. Rev.*, **144**, 1161–1177, doi:10.1175/MWR-D-15-0208.1.

Shrestha, P., A. P. Barros, and A. Khlystov, 2010: Chemical composition and aerosol size distribution of the middle mountain range in the Nepal Himalayas during the 2009 pre-monsoon season. *Atmos. Chem. Phys.*, **10**, 11 605–11 621, doi:10.5194/acp-10-11605-2010.

Skamarock, W. C., and Coauthors, 2008: A description of the Advanced Research WRF version 3. NCAR Tech. Note NCAR/TN-475+STR, 113 pp., doi:10.5065/D68S4MVH.

Smith, R. B., 1979: The influence of mountains on the atmosphere. *Advances in Geophysics*, Vol. 21, Academic Press, 87–230, doi:10.1016/S0065-2687(08)60262-9.

Smolarkiewicz, P. K., and R. Rotunno, 1989: Low Froude number flow past three-dimensional obstacles. Part I: Baroclinically generated lee vortices. *J. Atmos. Sci.*, **46**, 1154–1164, doi:10.1175/1520-0469(1989)046<1154:LFNFPT>2.0.CO;2.

——, and ——, 1990: Low Froude number flow past three-dimensional obstacles. Part II: Upwind flow reversal zone. *J. Atmos. Sci.*, **47**, 1498–1511, doi:10.1175/1520-0469(1990)047<1498:LFNFPT>2.0.CO;2.

Sun, X., and A. P. Barros, 2012: The impact of forcing datasets on the high-resolution simulation of Tropical Storm Ivan (2004) in the southern Appalachians. *Mon. Wea. Rev.*, **140**, 3300–3326, doi:10.1175/MWR-D-11-00345.1.

——, and ——, 2014: High resolution simulation of Tropical Storm Ivan (2004) in the southern Appalachians: Role of planetary boundary layer schemes and cumulus parameterization. *Quart. J. Roy. Meteor. Soc.*, **140**, 1847–1865, doi:10.1002/qj.2255.

——, and ——, 2015a: Isolating the role of surface evapotranspiration on moist convection along the eastern flanks of the tropical Andes using a quasi-idealized approach. *J. Atmos. Sci.*, **72**, 243–261, doi:10.1175/JAS-D-14-0048.1.

——, and ——, 2015b: Impact of Amazonian evapotranspiration on moisture transport and convection along the eastern flanks of the tropical Andes. *Quart. J. Roy. Meteor. Soc.*, **141**, 3325–3343, doi:10.1002/qj.2615.

Tao, J., and A. P. Barros, 2013: Prospects for flash flood forecasting in mountainous regions—An investigation of Tropical Storm Fay in the southern Appalachians. *J. Hydrol.*, **506**, 69–89, doi:10.1016/j.jhydrol.2013.02.052.

——, and ——, 2014: Coupled prediction of flood response and debris flow initiation during warm- and cold-season events in the southern Appalachians, USA. *Hydrol. Earth Syst. Sci.*, **18**, 367–388, doi:10.5194/hess-18-367-2014.

——, and ——, 2017: Multi-year atmospheric forcing datasets for hydrologic modeling in regions of complex terrain—Methodology and evaluation over the Integrated Precipitation and Hydrology Experiment 2014 domain. *J. Hydrol.*, doi:10.1016/j.jhydrol.2016.12.058, in press.

Thornthwaite, C. W., 1948: An approach toward a rational classification of climate. *Geogr. Rev.*, **38**, 55–94, doi:10.2307/210739.

Tokay, A., W. Petersen, P. Gatlin, and M. Wingo, 2013: Comparison of raindrop size distribution measurements by collocated disdrometers. *J. Atmos. Oceanic Technol.*, **30**, 1672–1690, doi:10.1175/JTECH-D-12-00163.1.

——, D. B. Wolff, and W. A. Petersen, 2014: Evaluation of the new version of the laser-optical disdrometer, OTT PARSIVEL². *J. Atmos. Oceanic Technol.*, **31**, 1276–1288, doi:10.1175/JTECH-D-13-00174.1.

Trenberth, K., 1991: Climate diagnostics from global analyses: Conservation of mass in ECMWF analyses. *J. Climate*, **4**, 707–722, doi:10.1175/1520-0442(1991)004<0707:CDFGAC>2.0.CO;2.

Wagner, J. S., A. Gohm, and M. W. Rotach, 2015: The impact of valley geometry on daytime thermally driven flows and vertical transport processes. *Quart. J. Roy. Meteor. Soc.*, **141**, 1780–1794, doi:10.1002/qj.2481.

Wallace, J. M., 1983: The climatological mean stationary waves: Observational evidence. *Large-Scale Dynamical Processes in the Atmosphere*, B. Hoskins and R. Pearce, Eds., Academic Press, 27–53.

Whiteman, C. D., 2000: *Mountain Meteorology: Fundamentals and Applications.* Oxford University Press, 355 pp.

Wilson, A. M., and A. P. Barros, 2014: An investigation of warm rainfall microphysics in the southern Appalachians: Orographic enhancement via low-level seeder−feeder interactions. *J. Atmos. Sci.*, **71**, 1783–1805, doi:10.1175/JAS-D-13-0228.1.

——, and ——, 2015: Landform controls on low level moisture convergence and the diurnal cycle of warm season orographic rainfall in the southern Appalachians. *J. Hydrol.*, **531**, 475–493, doi:10.1016/j.jhydrol.2015.10.068.